Available online at www.sciencedirect.com
ScienceDirect

Comput. Methods Appl. Mech. Engrg. 318 (2017) 349–381

Computer methods in applied mechanics and engineering

www.elsevier.com/locate/cma

A Peridynamics-SPH modeling and simulation of blast fragmentation of soil under buried explosive loads

Houfu Fan[a,b], Shaofan Li[a,*]

[a] *Department of Civil and Environmental Engineering, University of California, Berkeley, CA 94720, USA*
[b] *Livermore Software Technology Corporation, CA 94551, USA*

Received 22 March 2016; received in revised form 10 January 2017; accepted 20 January 2017
Available online 6 February 2017

Highlights

- Novel state-based Peridynamics formulation for geo-material models.
- Successful large scale simulation of explosive fragmentation of soil up to five million particles.
- Predictive simulation of soil fragmentation.
- Simulation of soil jet bursting out the soil bubble becoming soil ejecta.
- Novel computational algorithm for coupling Peridynamics and SPH.

Abstract

In this work, we report a computational study on Peridynamics modeling and simulation of soil fragmentation under buried explosive loads. We have implemented several geomaterial models of soil in the state-based Peridynamics formulation, which can take into account of the effects of strain softening, viscoplasticity, and porosity of soil. Moreover, we adopted a particle decohesion algorithm in the state-based Peridynamics for finite deformation to simulate soil fragmentation. A key technical ingredient of the simulation is the coupling between soil and explosive modeling methods, which is accomplished by coupling the state-based Peridynamics (soil) model with a modified smooth particle hydrodynamics (SPH) model (explosive). The modified SPH formulation used here is a non-local consistent particle dynamics that is formulated in the current (spatial) configuration.

Numerical results of the simulations are compared with the measured experimental data. It has been found that there is a general agreement between the simulation results and the experimental data, and the computational model developed here has shown certain predictive capacity.

Keywords: Blast load; Fragmentation; Granular material; Peridynamics; Smoothed Particle Hydrodynamics (SPH); Soil kinematics

---

[*] Corresponding author.
E-mail address: shaofan@berkeley.edu (S. Li).

http://dx.doi.org/10.1016/j.cma.2017.01.026

1. Introduction

Understanding dynamic behaviors of soil under blast loads is very important in many engineering applications, especially in some geotechnical engineering applications such as explosive protected constructions, earthquake simulations, military vehicle design, performance, and operation, disaster mitigation, and mining and land extractions, etc.

Dynamic behaviors of soil under buried explosive loading have been extensively studied in the past three decades, e.g. [1–14], among many others. However, to date, many crucial aspects of the physical process are still not well understood. Soil is a mixture of sand, rock, and clay with multiscale microstructure of different sizes and shapes, which may be considered as a cohesive and porous assemblage of individual solid particles that form a three-dimensional network of soil skeleton. In soil, water and air may also be filled inside the voids and pores of the soil skeleton, and we often refer the soil medium that has water saturation as saturated soil.

From the modeling perspective, it would be more accurate to model the soil as a non-local medium rather than a local continuum, because of the long range interaction among soil particles. During an underground explosion, a rapid release of energy from the buried explosive will generate the shock wave that is characterized by a sudden rise of pressure at the shock wave front, and it then propagates away from the explosion site. The interaction between the shock wave and soil particle aggregates will create massive fragmentation of the soil skeleton.

It has been a long standing open problem to accurately predict dynamic soil behaviors under the blast loading. To date, the best modeling and simulation of soil fragmentation under buried explosives is still based on empirical formulas from field tests and experiments e.g. [13,15,16], which fail to provide consistent prediction capability because of random data scattering. Moreover, since soil fragmentation is a typical nonlocal multiphase and multiscale phenomenon, discrepancy between simulation prediction based on local continuum geophysics and experimental measurement has been remarkably large.

Recently, efforts have been made to model the soil medium as nonlocal cohesive medium by using the state-based Peridynamics [17,18]. The advantages of such approach are: (1) it provides a nonlocal formulation that captures a main characterization of soil medium; (2) it offers an intrinsic numerical treatment for soil decohesion and fragmentation, and (3) the strong form of the mathematical formulation facilitates fast computation.

In specific, we have developed a state-based Peridynamics and smooth particle hydrodynamics (SPH) coupling method to simulate massive soil fragmentation due to buried explosives. Some preliminary results have been reported in [17–19], in which, however, some technical details of the simulation are missing. Peridynamics is a nonlocal reformulation of continuum mechanics [20,21], and it is particular suitable in modeling and simulation of granular materials such as soil, concrete materials, and particulate materials in general. In this work, we focus on non-local continuum modeling of soil, and present a systematical presentation on peridynamics/SPH simulation of soil fragmentation due to the blast loading generated by buried explosive charges.

Different from the previous study, the following progresses that have been made in this work: (**1**) Besides the uncapped Drucker–Prager model is used to model soil medium, in the present study, we add two other geomaterial models: (a) the Drucker–Prager Cap (DPC) model [22,23], which can model the strain-softening behavior of soil when plastic volume strain occurs on the cone, and (b) the Arenisca model [24–26], which is a semi-empirical geomaterial model that can make empirical adjustments to soil's bulk modulus to take into account liquid filled porous effects under high strain rate loadings. Moreover it uses an overstress model to include viscoplasticity effect, and employs a void disaggregation algorithm to account for the added volume when grains disaggregate under explosive loading; (**2**) Focusing on simulation of soil fragmentation, we developed a modified Peridynamics soil particle decohesion criterion to capture pressure-driven fragmentation process at the center of explosion site; (**3**) A main challenge of using the state-based Peridynamics is to enforce the objectivity of the computational algorithm, because as a total Lagrangian based particle method, the state-based Peridynamics is prone to violate the principle of material frame indifference. We have implemented the Hughes–Winget algorithm to integrate Peridynamics equations of motion to ensure the objectivity or frame-indifference of the Peridynamics constitutive models; (**4**) We have studied the irregular particle distribution effect on the Peridynamics simulation, and (**5**) We have developed a parallel Peridynamics simulation tool to conduct large scale simulations that is up to five million particles.

The paper is organized into six sections. In Section 2, we start the presentation by a brief review on the two particle methods and their coupling scheme. In Section 3, three geomaterial material models are presented, and the Hughes–Winget algorithm is rephrased in the framework of nonlocal state-based Peridynamics, in order to achieve the objective requirement in time integration. In Section 4, several numerical examples are presented. First, a three-dimensional

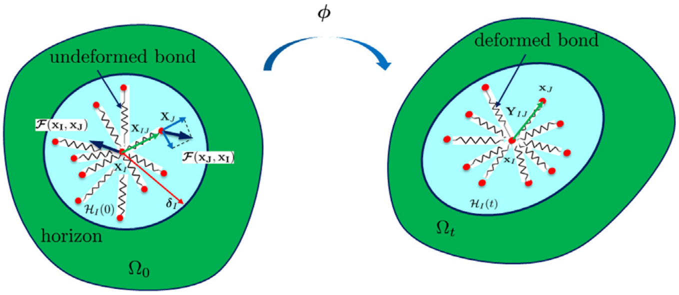

Fig. 1. Schematic illustration of the state-based Peridynamics: A nonlocal particle method with non-ordinary material bonds.

column is prescribed with uniaxial compression, to verify the Peridynamics model and the corresponding numerical implementation. Second, two numerical tests are conducted to demonstrate the objectivity of the time integration algorithm for the state-based Peridynamics soil models. Finally, by using the proposed PD-SPH coupling algorithm, we present the simulation of soil fragmentation/ejection induced by the blastic loadings of buried explosive. The comparison of the early soil deformations from an explosion experiment and the corresponding simulation results demonstrate the validity of the Peridynamics soil models, as well as the capability of the Peridynamics/SPH coupling scheme. We close our presentation with discussions in Section 5.

2. State-based Peridynamics, SPH, and their coupling

In this section, we first review the state-based Peridynamics method and the smoothed particle hydrodynamics (SPH) method, and then we discuss the coupling algorithm of the two methods.

2.1. Basic formulations of state-based peridynamics

The state-based Peridynamics theory was first introduced by Silling et al. [21], which is a reformulation of nonlocal continuum mechanics. Consider a continuum domain Ω_0 that is discretized into a set of material particles $\mathbf{X}_I$ with associated volume V_I^0 and mass density ρ_I^0, where $I = 1, 2, \ldots, N$ as shown in Fig. 1. A material particle $\mathbf{X}_I$ only interacts with those particle $\mathbf{X}_J$ within a local region, called the horizon $\mathcal{H}_I$ whose radius is $\delta_{\mathbf{X}_I}$.

The relative position vector pointing from particle $\mathbf{X}_I$ to $\mathbf{X}_J$ in the reference configuration is called a bond, which shall be denoted as

$$\mathbf{X}_{IJ} := \mathbf{X}_J - \mathbf{X}_I. \tag{1}$$

Subjected to certain motion or deformation $\boldsymbol{\phi}$, the continuum body deforms and the bond $\mathbf{X}_{IJ}$ in the reference configuration becomes

$$\mathbf{x}_{IJ} := \mathbf{x}_J - \mathbf{x}_I = \underline{\mathbf{Y}}(\mathbf{X}_{IJ}) \tag{2}$$

where $\underline{\mathbf{Y}}$ is a nonlinear quantity called the deformation state, similar to a tensor in classical continuum mechanics. Here, the deformation state $\underline{\mathbf{Y}}$ maps the undeformed bond $\mathbf{X}_{IJ}$ to a deformed bond $\mathbf{x}_{IJ}$.

In the Peridynamics theory, the balance of the linear momentum is read as (see [27]),

$$\rho_I^0 \ddot{\mathbf{u}}_I = -\int_{\mathcal{H}_{\mathbf{X}_I}} \left[\underline{\mathbf{T}}^{JI}[\mathbf{X}_J, t]\langle \mathbf{X}_{IJ}\rangle + \underline{\mathbf{T}}^{IJ}[\mathbf{X}_I, t]\langle \mathbf{X}_{IJ}\rangle\right] dV_J + \rho_I^0 \mathbf{b}_I, \tag{3}$$

where $\underline{\mathbf{T}}$ is the force state, $\mathbf{u}$ is the displacement and $\mathbf{b}$ is the external body force. In computations, Eq. (8) is discretized into the following algebraic equation,

$$\rho_I^0 \ddot{\mathbf{u}}_I = -\sum_{J=1}^{N_I} \left[\underline{\mathbf{T}}^{JI}[\mathbf{X}_J, t]\langle \mathbf{X}_{BA}\rangle + \underline{\mathbf{T}}^{IJ}[\mathbf{X}_I, t]\langle \mathbf{X}_{IJ}\rangle\right] V_J^0 + \rho_I^0 \mathbf{b}_I, \tag{4}$$

where V_J^0 is the volume associated with the particle J.

The force state can be expressed in terms of the first Piola–Kirchhoff (PK1) stress as

$$\underline{\mathbf{T}}^{JI}[\mathbf{X}_J, t]\langle \mathbf{X}_{JI}\rangle = \omega(|\mathbf{X}_{JI}|)\mathbf{P}_J\mathbf{K}_J^{-1}\cdot\mathbf{X}_{JI}, \tag{5}$$

$$\underline{\mathbf{T}}^{IJ}[\mathbf{X}_I, t]\langle \mathbf{X}_{IJ}\rangle = \omega(|\mathbf{X}_{IJ}|)\mathbf{P}_I\mathbf{K}_I^{-1}\cdot\mathbf{X}_{IJ}, \tag{6}$$

where $\mathbf{P}_I$ and $\mathbf{P}_J$ are the first Piola–Kirchhoff stress of the particle I and J respectively; $\omega(|\mathbf{X}_{IJ}|)$ is a positive scalar influence function of $|\mathbf{X}_{IJ}|$, and $\mathbf{K}_I$ is the reference shape tensor that is defined as

$$\mathbf{K}_I := \int_{\mathcal{H}_{\mathbf{X}_I}} \omega(|\mathbf{X}_{IJ}|)\mathbf{X}_{IJ}\otimes\mathbf{X}_{IJ} dV_I. \tag{7}$$

If the horizon size of the particle I is the same as that of the particle J, for quasi-uniform particle distributions, we have $\mathbf{K}_I = \mathbf{K}_J$. We can then rewrite Eqs. (8) and (9) as follows,

$$\rho_I^0\ddot{\mathbf{u}}_I = \int_{\mathcal{H}_{\mathbf{X}_I}} \omega(|\mathbf{X}_{IJ}|)(\mathbf{P}_J - \mathbf{P}_I)\mathbf{K}_I^{-1}\cdot\mathbf{X}_{IJ}, dV_J + \rho_I^0\mathbf{b}_I, \tag{8}$$

$$\rho_I^0\ddot{\mathbf{u}}_I = \sum_{J=1}^{N_I}\omega(|\mathbf{X}_{IJ}|)(\mathbf{P}_J - \mathbf{P}_I)\mathbf{K}_I^{-1}\cdot\mathbf{X}_{IJ}V_J^0 + \rho_I^0\mathbf{b}_I. \tag{9}$$

To find the local stress at each material point, we need to find the nonlocal strain or deformation gradient first. To do so, we first define a nonlocal two-point shape tensor $\mathbf{N}_I$ on a local linear space of manifolds $\Omega_t \times \Omega_0$ as,

$$\mathbf{N}_I := \int_{\mathcal{H}_{\mathbf{X}_I}} \omega(|\mathbf{X}_{IJ}|)\mathbf{x}_{IJ}\otimes\mathbf{X}_{IJ} dV_J. \tag{10}$$

As a first order approximation, we may assume that

$$\mathbf{x}_{IJ} = \underline{\mathbf{Y}}(\mathbf{X}_{IJ}) = \mathbf{F}_I\cdot\mathbf{X}_{IJ}, \tag{11}$$

where $\mathbf{F}_I$ is the deformation gradient at the particle I. Substituting Eq. (11) into (10), we then have,

$$\mathbf{N}_I = \mathbf{F}_I\cdot\left[\sum_{\mathbf{X}_J\in\mathcal{H}_{\mathbf{X}_I}} \omega(|\mathbf{X}_{IJ}|)\mathbf{X}_{IJ}\otimes\mathbf{X}_{IJ}V_J^0\right] = \mathbf{F}_I\cdot\mathbf{K}_I. \tag{12}$$

Now we obtain the nonlocal deformation gradient at the material point I in terms of its shape tensors,

$$\mathbf{F}_I = \mathbf{N}_I\cdot\mathbf{K}_I^{-1}, \tag{13}$$

without taking analytical derivatives at the local position.

Remark 1. **1.** Eq. (8) is in fact different from the original (formal) state-based Peridynamics formulation derived in [21]. From the perspective of computational formulation, Eq. (8) is similar to the collocation form of the wavelet reproducing kernel particle method (RKPM) [28–30]. The derivation of Eq. (8) is based on [27];

2. From the perspective of physical modeling, the state-based Peridynamics may be viewed as a macroscale analog of the soft sphere type of discrete element method (DEM) [31]. The major difference is that in the soft sphere DEM the interaction between two particles behaves more like colloidal cohesive-frictional contact force, whereas in the state-based Peridynamics it behaves more like "material bond force" (See Fig. 1), and

3. The type of the state-based Peridynamics that we are dealing with in this work is called the non-ordinary state-based Peridynamics, because the interaction force between the two material particles is not along the direction of the relative position vector, i.e. $\mathbf{X}_{IJ}$. It contains both normal parallel component as well as perpendicular component (see Fig. 1). This feature also is shared by some DEM formulations, e.g. [32].

2.2. *Peridynamics particle decohesion algorithm*

In the state-based Peridynamics, if the change of a material bond length exceeds a critical value, the bond will break or it will be disabled in computations. This critical value is called the "critical bond stretch" s_0 that is defined as,

$$s_0 = \frac{|\mathbf{x}_{IJ}| - |\mathbf{X}_{IJ}|}{|\mathbf{X}_{IJ}|}. \tag{14}$$

In the linear elastic bond-based Peridynamics material model, the critical bond stretch s_0 [20] is defined as

$$s_0 = \sqrt{\frac{5G_0}{9c\delta}}, \tag{15}$$

where G_0 is the energy release rate, c is the micro modulus, and δ is the radius of the horizon for the particle under consideration. In the current work, the critical bond length is chosen as an empirical value, which is modified along with a set of parameters to calibrate the experiment data.

For given the critical stretch s_0, the damage at any material point is defined as

$$\phi(\mathbf{X}, t) = 1 - \frac{\int_{\mathcal{H}_{\mathbf{X}_I}} \mu(\mathbf{x}, t) dV}{\int_{\mathcal{H}_{\mathbf{X}_I}} dV}, \tag{16}$$

where

$$\mu(\mathbf{x}, t) = \begin{cases} 1, & \text{if } s < s_0 \\ 0, & \text{otherwise.} \end{cases} \tag{17}$$

Note that the function μ is defined for each material bond, and the damage parameter $\phi(\mathbf{X}, t)$ is defined for a given material point, which usually will connect to many material bonds.

2.3. A consistent smoothed particle hydrodynamics (SPH) for explosive gas

The SPH method was initially developed for solving hydrodynamics problems. There are two key ingredients in the formulation of the SPH methodology: kernel approximation and particle approximation [33].

In the SPH method, a continuous field $f(\mathbf{x})$ and its gradient $\nabla f(\mathbf{x})$ is approximated as

$$\langle f(\mathbf{x}) \rangle = \int_{\Omega} f(\mathbf{y}) w(|\mathbf{x} - \mathbf{y}|) dV_{\mathbf{y}} \tag{18}$$

where $\langle\rangle$ is the kernel approximation operator [34], w is the so-called kernel function. Using the smoothing function, the gradient of $f(\mathbf{x})$ can be written as

$$\langle \nabla f(\mathbf{x}) \rangle = \int_{\Omega} f(\mathbf{y}) \nabla_{\mathbf{x}} w(|\mathbf{x} - \mathbf{y}|) dV_{\mathbf{y}} \tag{19}$$

where the minus sign results from the integration by parts, which is standard in SPH [35]. The discretized forms of Eqs. (18) and (19) are

$$\langle f(\mathbf{x}_I) \rangle = \sum_{\mathbf{x}_J \in \mathcal{S}_{\mathbf{x}_I}} f(\mathbf{x}_J) w(|\mathbf{x}_I - \mathbf{x}_J|) V_J \tag{20}$$

and

$$\langle \nabla f(\mathbf{x}_I) \rangle = \sum_{\mathbf{x}_J \in \mathcal{S}_{\mathbf{x}_I}} f(\mathbf{x}_J) \nabla_{\mathbf{x}_I} w(|\mathbf{x}_{IJ}|) V_J \tag{21}$$

where $\mathcal{S}_{\mathbf{x}_I}$ represents the supporting (influence) domain of particle $\mathbf{x}_I$, similar to the horizon $\mathcal{H}_{\mathbf{X}_I}$ in the state-based Peridynamics.

With these preparations, we can now cast the SPH equations of motion of the explosive as,

$$\frac{D\rho_I}{Dt} = - \sum_{\mathbf{x}_J \in \mathcal{S}_{\mathbf{x}_A}} m_J (\mathbf{v}_J - \mathbf{v}_I) \cdot \nabla_{\mathbf{x}_I} w(|\mathbf{x}_{IJ}|) \tag{22}$$

$$\frac{D\mathbf{v}_I}{Dt} = - \sum_{\mathbf{x}_J \in \mathcal{S}_{\mathbf{x}_I}} m_J \left(\frac{p_I}{\rho_I^2} + \frac{p_J}{\rho_J^2} + \Pi_{IJ} \right) \nabla_{\mathbf{x}_I} w(|\mathbf{x}_{IJ}|) \tag{23}$$

$$\frac{De_I}{Dt} = \frac{1}{2} \sum_{\mathbf{x}_J \in \mathcal{S}_{\mathbf{x}_I}} m_B \left(\frac{p_I}{\rho_I^2} + \frac{p_J}{\rho_J^2} + \Pi_{IJ} \right) (\mathbf{v}_J - \mathbf{v}_I) \cdot \nabla_{\mathbf{x}_I} w(|\mathbf{x}_{IJ}|) \tag{24}$$

$$\frac{D\mathbf{x}_I}{Dt} = \mathbf{v}_I \tag{25}$$

where ρ, $\mathbf{v}$, e, p are the density, velocity, internal energy and pressure at the corresponding particle. $\frac{D()}{dt}$ represents the time derivative of the quantity in the bracket. Π_{IJ} is the standard Monaghan viscosity [36], which can be written as (e.g. [37]),

$$\Pi^{IJ} = \begin{cases} \dfrac{-\alpha \bar{c}_{IJ} \mu_{IJ} + \beta \mu_{IJ}^2}{\bar{\rho}_{IJ}}, & \mathbf{v}_{IJ} \cdot \mathbf{x}_{IJ} < 0; \\ 0, & \mathbf{v}_{IJ} \cdot \mathbf{x}_{IJ} > 0; \end{cases} \tag{26}$$

with

$$\mu_{IJ} = \frac{\bar{h}_{IJ} \mathbf{v}_{IJ} \cdot \mathbf{x}_{IJ}}{(\mathbf{x}_{IJ})^2 + \eta^2 \bar{h}_{IJ}^2}, \tag{27}$$

where $\alpha \sim 1$ and $\beta \sim 2$ are artificial constants; $\bar{\rho}$ is the average density, $\bar{c}_{IJ}$ is the average particle speed; $\eta \sim 0.1$, and h_{IJ} are the average smoothing length (radius of the support), i.e.

$$\bar{c}_{IJ} = \frac{1}{2}(c_I + c_J), \;\; \bar{\rho}_{IJ} = \frac{1}{2}(\rho_I + \rho_J), \;\text{and}\; \bar{h}_{IJ} = \frac{1}{2}(h_I + h_J). \tag{28}$$

The original SPH method has an intrinsic flaw, i.e. it is not a partition of unity after the discretization. Consequently, the derivative of its window function $w(|\mathbf{x}_J - \mathbf{x}_I|)$ does not form a partition of nullity after the discretization, which causes issues in both interpolation consistency and numerical stability. This is because the governing equations of SPH, i.e. Eqs. (23)–(25), depend on the local derivatives or the local spatial gradient of the window function.

In this work, we construct a consistent modified SPH derivative field by introducing the following nonlocal gradient. Consider a vector (or tensor) field $\mathbf{f}(\mathbf{x})$ in the current configuration. We can define a nonlocal spatial gradient field of the vector field $\mathbf{f}(\mathbf{x})$ as (see [27] for details),

$$\nabla_{\mathbf{x}} \otimes [\mathbf{f}(\mathbf{x})] := \left\{ \int_{\mathcal{S}_{\mathbf{x}}} w(|\mathbf{y} - \mathbf{x}|) \, [\mathbf{f}(\mathbf{y}) - \mathbf{f}(\mathbf{x})] \otimes (\mathbf{y} - \mathbf{x}) \, dv \right\} \mathbf{M}_{\mathbf{x}}^{-1}, \tag{29}$$

where the shape tensor in the current configuration is defined as

$$\mathbf{M}_{\mathbf{x}} := \int_{\mathcal{S}_{\mathbf{x}}} w(|\mathbf{y} - \mathbf{x}|) \, (\mathbf{y} - \mathbf{x}) \otimes (\mathbf{y} - \mathbf{x}) \, dv, \tag{30}$$

in which $w(|\mathbf{y} - \mathbf{x}|)$ is the SPH window function that depends on the relative distance of two particles $\mathbf{x}$ and $\mathbf{y}$ in the current configuration. Eq. (29) can then be converted into discrete form as follows,

$$\nabla_{\mathbf{x}} \otimes [\mathbf{f}(\mathbf{x}_I)] := \left\{ \sum_{\mathbf{x}_J \in \mathcal{S}_{\mathbf{x}_I}} \frac{1}{\rho_J} w(|\mathbf{x}_{IJ}|) \, [\mathbf{f}_J - \mathbf{f}_I] \otimes (\mathbf{x}_{IJ}) \, m_J \right\} \mathbf{M}_I^{-1}. \tag{31}$$

Notice that the divergence of a vector or tensor field can be also constructed with the same strategy by replacing "⊗" with "·" in the respective equations, i.e. we can define a nonlocal divergence operation as,

$$\nabla_{\mathbf{x}} \cdot [\mathbf{f}(\mathbf{x})] := \left\{ \int_{\mathcal{S}_{\mathbf{x}}} w(|\mathbf{y} - \mathbf{x}|) \, [\mathbf{f}(\mathbf{y}) - \mathbf{f}(\mathbf{x})] \cdot \left((\mathbf{y} - \mathbf{x}) \, \mathbf{M}_{\mathbf{x}}^{-1} \right) dv \right\}, \tag{32}$$

whose discrete form is expressed as

$$\nabla_{\mathbf{x}} \cdot [\mathbf{f}(\mathbf{x}_I)] := \left\{ \sum_{\mathbf{x}_J \in \mathcal{S}_{\mathbf{x}_I}} \frac{1}{\rho_J} w(|\mathbf{x}_{IJ}|) \, [\mathbf{f}_J - \mathbf{f}_I] \cdot \left((\mathbf{x}_{IJ}) \, \mathbf{M}_I^{-1} \right) m_J \right\}. \tag{33}$$

We call these gradient and divergence operators of a vector or tensorial field (defined on a finite number of material points) as discrete differential operators. With these discrete differential operators, we can replace the corresponding

Table 1
EOS material parameters of the C4 charge (m kg s units).

ρ	A	B	R1	R2	ω	E
1601	5.98×10^{11}	1.38×10^{9}	4.5	1.5	0.32	8.70×10^{9}

SPH governing equations of the conservation laws (mass, momentum, energy) with the following consistent hydrodynamics equations,

$$\frac{D\rho_I}{Dt} = -\sum_{\mathbf{x}_J \in \mathcal{S}_{\mathbf{x}_I}} m_J(\mathbf{v}_J - \mathbf{v}_I)\cdot w(|\mathbf{x}_{IJ}|)\mathbf{x}_{IJ}\mathbf{M}_I^{-1}, \tag{34}$$

$$\frac{D\mathbf{v}_I}{Dt} = -\sum_{\mathbf{x}_J \in \mathcal{S}_{\mathbf{x}_I}} m_J\left(\frac{p_I}{\rho_I^2} + \frac{p_J}{\rho_J^2} + \Pi_{IJ}\right) w(|\mathbf{x}_{IJ}|)\mathbf{x}_{IJ}\mathbf{M}_I^{-1}, \tag{35}$$

$$\frac{De_I}{Dt} = \frac{1}{2}\sum_{\mathbf{x}_J \in \mathcal{S}_{\mathbf{x}_A}} m_J\left(\frac{p_I}{\rho_I^2} + \frac{p_J}{\rho_J^2} + \Pi_{IJ}\right)\cdot w(|\mathbf{x}_{IJ}|)(\mathbf{v}_J - \mathbf{v}_I)\cdot \mathbf{x}_{IJ}\mathbf{M}_I^{-1}, \tag{36}$$

$$\frac{D\mathbf{x}_I}{Dt} = \mathbf{v}_I. \tag{37}$$

Thus the dependence of the kernel function is successfully eliminated, and the modified SPH formula becomes consistent with that of the state-based Peridynamics.

In this work, the pressure of the explosive is obtained from the equation of state. The Jones–Wilkins–Lee (JWL) equation of state is used for the C4 explosive charge, which is defined as,

$$p = A\left(1 - \frac{\omega}{R_1 dF}\right)e^{-R_1 dF} + B\left(1 - \frac{\omega}{R_2 dF}\right)e^{-R_2 dF} + \frac{\omega e}{V}, \tag{38}$$

where p is the pressure, V is the volume, w is the Gruneisen parameter, dF is the volume ratio $\frac{V}{V_0}$ (V_0 is the initial volume) and A, R_1, B, R_2, ω. The specific constants of the C4 charge used in the computation are given in Table 1.

The material parameters for the soil and C4 charge are taken from [38].

2.4. Coupling of Peridynamics and SPH

The state-based Peridynamics has been mainly used to model solid or granule materials, because it has a bond breaking feature that can model decohesion between solid particles, whereas SPH is primarily used to model fluids, even though occasionally it was used to model solids as well. In those cases, the shortcomings of SPH such as tensile instability and lack of consistency in interpolation field may become obvious. Therefore, in the soil fragmentation simulation, we choose the state-based Peridynamics to model soil medium, while using a modified SPH method to model the explosive. Therefore, a crucial step in the simulation is how to couple the two different methods to ensure a seamless interaction between soil particles and explosive gas. From computational perspective, both Peridynamics and SPH are nonlocal strong form particle methods. In fact the modified SPH method outlined in the previous section can be viewed as a "Peridynamics" in the current configuration, or an updated Lagrangian form of Peridynamics [27]. This affinity between the two methods provides an easy coupling scheme of the two methods.

In Fig. 2, we show a schematic illustration at the interface of Peridynamics (blue) domain and SPH (red) domain. One can see that near the interface of the two domain, there are SPH particles (red) in a Peridynamics particle's horizon, and vice versa there are Peridynamics particles inside a support of an SPH particle. To couple the two methods, if an SPH particle is inside the horizon of a Peridynamics $\mathbf{X}_J \in \mathcal{H}_{\mathbf{X}_I}$, one may simply treat it as a "Peridynamics" particle by constructing the same influence function $\omega(|\mathbf{X}_{IJ}|)$, and the shape tensors $\mathbf{K}_J$, $\mathbf{N}_J$. Combining Eqs. (8)–(13), we can find the force acting on a Peridynamics particle as

$$\mathcal{F}_I = \sum_{\mathbf{X}_J \in \mathcal{H}_{\mathbf{X}_I}} \left[\omega(|\mathbf{X}_{IJ}|)(\mathbf{P}_J - \mathbf{P}_I)\mathbf{K}_I^{-1}\cdot \mathbf{X}_{IJ}\right] V_J^0. \tag{39}$$

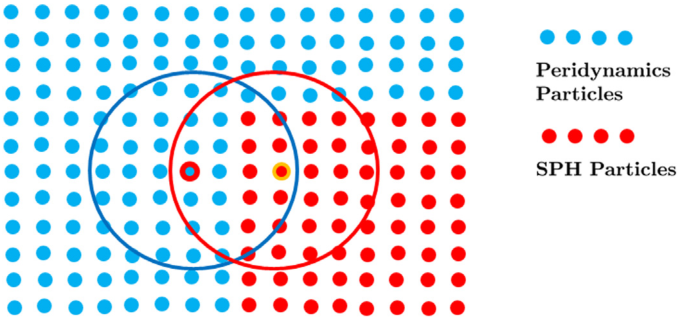

Fig. 2. Schematic illustration of the coupling scheme of Peridynamics particles and SPH particles. (For interpretation of the references to color in this figure legend, the reader is referred to the web version of this article.)

To fake an SPH particle as a Peridynamics particle, the only state variable unknown is the first Piola–Kirchhoff stress tensor $\mathbf{P}_I$ of the particle, which can be partially recovered by using the pressure value of the SPH particle, i.e.

$$\mathbf{P}_J = J_J p_J \mathbf{F}_J^{-T} \tag{40}$$

where p_J is the pressure, $\mathbf{F}_J$ is the deformation gradient at particle $\mathbf{X}_J$ and $J_J = \det[\mathbf{F}_J]$.

On the other hand, when a Peridynamics particle is inside the support of an SPH particle, we shall treat (pretend) it as an SPH particle, and the corresponding SPH quantities of the Peridynamics particle, such as the density ρ_J, velocity $\mathbf{v}_J$ and pressure p_J are needed, in order to perform the SPH calculations, i.e. the integration of SPH hydrodynamics equations (22)–(25). First, the velocity $\mathbf{v}_J$ is always available. In addition, other related variables can also be calculated based on the following formulas:

$$(1)\ \text{Density :}\quad \rho_J = \frac{1}{J_I}\rho_J^0, \tag{41}$$

and

$$(2)\ \text{Pressure :}\quad p_J = 1/3\mathrm{tr}(\boldsymbol{\sigma}_J) = 1/(3J_J)\mathrm{tr}(\mathbf{P}_J\mathbf{F}_J^T), \tag{42}$$

where ρ_J^0 is the initial density at particle $\mathbf{X}_J$.

To this end, one more technical ingredient is still needed to determine the nonlinear cohesive-frictional spring force between two material or soil particles. In the state-based Peridynamics, this is done by incorporated the macroscale phenomenological constitutive model into the Peridynamics formulation, i.e. once we determine the nonlocal deformation gradient, we shall use the phenomenological geomaterial constitutive relation to determine stress state (the first Piola–Kirchhoff stress $\mathbf{P}_I$ and $\mathbf{P}_J$), and then evaluate the bond force,

$$\mathcal{F}_I = \omega(|\mathbf{X}_{IJ}|)(\mathbf{P}_J - \mathbf{P}_I)\mathbf{K}_I^{-1}\cdot\mathbf{X}_{IJ}.$$

In the literature, several conventional constitutive material models have been implemented in the state-based Peridynamics for solids, such as hypoelastic model [39], hyperelastic model [21], viscoplastic model [40], continuum damage model such as the modified Johnson–Cook constitutive model [41], and among others. In this work, we shall implement several geomechanics models in the state-based Peridynamics formulation, which will be discussed in next section.

3. Soil constitutive modeling

In this section, we discuss how to model soil behaviors, and how to implement these constitutive models into Peridynamics formulation.

3.1. Drucker–Prager plasticity model (without cap)

The state-based Peridynamics can be termed as a nonlocal continuum theory with an integral equation formulation. Since that in the state-based Peridynamics, we can incorporate conventional macroscale stress–strain relation through the force state (see Eq. (6)) once the discrete deformation gradient is constructed. The existence of the internal force state is based on an equivalence or existence of the strain energy density function. As a granular material, soils usually present great nonlinearities after plastic yielding, with pressure-sensitive yield surfaces. In the literature, there are several successful constitutive models for soils, such as the Drucker–Prager (DP) model, the Mohr–Coulomb (MC) model and the Matsuoka–Nakai (MN) model. In this work, the Drucker–Prager (DP) plasticity model [22] is adopted to characterize the plastic behaviors of the soil. The DP model has been extensively used in numerical simulations of soil, rock and concrete structures [42]. The material parameters of the DP model for soils are well documented with experimental calibrations. In this section, we first give a brief review of the uncapped DP model, mainly focusing on the constitutive updates for a nonlinear finite deformation, which are then expressed in the corresponding Peridynamics formulation.

The yield function of the Drucker–Prager model is given as

$$\begin{cases} f = \|\mathbf{s}\| - (A(\phi')c' - B(\phi')p') \leq 0 \\[2ex] A(\phi') = \dfrac{2\sqrt{6}\cos\phi'}{3+\beta\sin\phi'} \\[2ex] B(\phi') = \dfrac{2\sqrt{6}\sin\phi'}{3+\beta\sin\phi'}, \quad -1 \leq \beta \leq 1 \end{cases} \tag{43}$$

where $\mathbf{s}$ is the deviatoric stress tensor i.e. $\mathbf{s} := \boldsymbol{\tau} - \frac{1}{3}\mathrm{tr}(\boldsymbol{\tau})\mathbf{I}$, c' is the effective cohesion (Pa), p' is the mean effective stress, and ϕ' the effective friction angle. We use $\beta = 1$ and $\beta = -1$ to approximate two cases of the Drucker–Prager model, i.e, the triaxial extension (TE) corners and the triaxial compression (TC) corners of the Mohr–Coulumb yield surface, respectively.

As a non-associative flow rule, the Drucker–Prager plastic potential function can be expressed as

$$\begin{cases} g = \|\mathbf{s}\| - (A(\psi')c' - B(\psi')p') \\[2ex] A(\psi') = \dfrac{2\sqrt{6}\cos\psi'}{3+\beta\sin\psi'} \\[2ex] B(\psi') = \dfrac{2\sqrt{6}\sin\psi'}{3+\beta\sin\psi'}, \quad -1 \leq \beta \leq 1 \end{cases} \tag{44}$$

where ψ' is the effective dilation angle. If $\phi' = \psi' = 0$, Eqs. (43) and (44) are the identical (the yield function and potential function overlaps), and the Drucker–Prager model reduces to a form similar to J_2 plasticity, which is very useful in approximating the shear strength of undrained soil.

The rate equation for the stress, evolution equations for the plastic flow and internal variables can be expressed as,

$$L_v\boldsymbol{\tau} = \mathbf{a} : (\mathbf{d} - \mathbf{d}^p); \tag{45}$$

$$\mathbf{d}^p = \dot{\gamma}\frac{\partial g}{\partial \boldsymbol{\tau}}; \tag{46}$$

$$\dot{\mathbf{q}}^\zeta = \dot{\gamma}\mathbf{H}\cdot\mathbf{h}(\boldsymbol{\tau}, \mathbf{q}^\zeta), \quad \text{and} \tag{47}$$

$$\mathbf{h} = -\frac{\partial f}{\partial \mathbf{q}^\zeta}, \tag{48}$$

where $L_v\boldsymbol{\tau}$ is the Lie derivative of the Kirchhoff stress tensor $\boldsymbol{\tau}$; $\mathbf{a} = \lambda\mathbf{I}\otimes\mathbf{I} + 2\mu\mathbb{I}$ is the spatial elasticity tensor with $\mathbf{I}$ as the second order unit tensor and $\mathbb{I}$ as the fourth order symmetric tensor; $\mathbf{d} = \frac{1}{2}\left(\boldsymbol{\ell} + \boldsymbol{\ell}^T\right)$; $\boldsymbol{\ell} = \dot{\mathbf{F}}\mathbf{F}^{-1}$ is the rate of deformation, $\mathbf{d}^p$ is the plastic rate of deformation, $\mathbf{h}$ is a hardening function and $\mathbf{q}^\zeta$ are the specific internal states. For the uncapped DP model, $\mathbf{q}^\zeta = \{c', \phi', \psi'\}^T$. For the sake of simplicity, it is assumed that the ISVs are to evolve under an independent, linear hardening/softening model, i.e.,

$$\mathbf{H} = \begin{bmatrix} H^c & 0 & 0 \\ 0 & H^\phi & 0 \\ 0 & 0 & H^\psi \end{bmatrix} \tag{49}$$

where H^c, H^ϕ, H^ψ are linear hardening/softening modulus for c', ϕ', ψ', respectively.

Based on the plastic potential function (see Eq. (44)), the evolution of plastic flow can be derived as

$$\begin{aligned}\mathbf{d}^p &= \dot{\gamma}\frac{\partial g}{\partial \boldsymbol{\tau}} = \dot{\gamma}\left(\frac{\partial \|\mathbf{s}\|}{\partial \boldsymbol{\tau}} + B(\psi')\frac{\partial p'}{\partial \boldsymbol{\tau}}\right)\\ &= \dot{\gamma}\left(\frac{\mathbf{s}}{\|\mathbf{s}\|} + \frac{1}{3}B(\psi')\mathbf{I}\right)\end{aligned}$$

where **I** is the second order identity tensor.

In Eq. (47), **h** is a hardening function. Using the maximum plastic dissipation principle, for the uncapped DP model, one can obtain

$$\mathbf{h} = \begin{pmatrix} A(\phi') \\ \dfrac{\partial A(\phi')}{\partial \phi'}c' - \dfrac{\partial B(\phi')}{\partial \phi'}p' \\ \dfrac{\partial A(\psi')}{\partial \psi'}c' - \dfrac{\partial B(\psi')}{\partial \psi'}p' \end{pmatrix}. \tag{50}$$

Using the consistency condition $\dot{f} = 0$, the plastic multiplier $\dot{\gamma}$ can be obtained as

$$\begin{cases} \dot{\gamma} = \dfrac{1}{\chi}\dfrac{\partial f}{\partial \boldsymbol{\tau}} : \mathbf{a} : \dot{\mathbf{d}} \\ \\ \chi = \dfrac{\partial f}{\partial \boldsymbol{\tau}} : \mathbf{a} : \dfrac{\partial g}{\partial \boldsymbol{\tau}} - \dfrac{\partial f}{\partial \mathbf{q}^{\zeta}} : \mathbf{H} \cdot \mathbf{h}. \end{cases} \tag{51}$$

Eqs. (45), (47) and (51) are the equations of constitutive update of a non-linear plastic constitutive model. The three sets of unknowns $(\boldsymbol{\tau}, \mathbf{q}^{\zeta}, \dot{\gamma})$ are coupled in the non-linear evolution equations, which can be solved by the Newton–Raphson iteration method. For simplicity, the following explicit update algorithm is adopted in this work,

$$\boldsymbol{\tau}_I^{\mathrm{tr}}(t_{n+1}) = \mathbf{f}_I(t_{n+1})\boldsymbol{\tau}_I(t_n)\mathbf{f}_I^T(t_{n+1}) + \mathbf{a}_I : (\mathbf{d}_I(t_{n+1})\Delta t) \tag{52}$$

$$f_{n+1}^{\mathrm{tr}} = \|\mathbf{s}^{\mathrm{tr}}\| - \left[A(\phi'_n)c'_n - B(\phi'_n)(p')^{\mathrm{tr}}_{n+1}\right] \tag{53}$$

where the superscript tr stands for the corresponding trial items. Note that in Eq. (52) we define

$$\mathbf{f}_I(t_{n+\alpha}) := \mathbf{I} + \alpha\tilde{\nabla}_n \Delta\mathbf{u}_I \tag{54}$$

where $\Delta\mathbf{u} = \mathbf{u}^{n+1} - \mathbf{u}^n$; $0 \le \alpha \le 1$; $\tilde{\nabla}_n$ is a nonlocal gradient operator, and we define

$$\mathbf{h}_I(t_n) := \tilde{\nabla}_n(\Delta\mathbf{u}_I) := \Big(\sum_{\mathbf{X}_J \in \mathcal{H}_{\mathbf{X}_A}} (\Delta\mathbf{u}_J - \Delta\mathbf{u}_I) \otimes \mathbf{x}_{IJ}^n V_J^0\Big)(\mathbf{K}_I^n)^{-1}, \tag{55}$$

where

$$\mathbf{K}_I^n := \sum_{\mathbf{X}_J \in \mathcal{H}_{\mathbf{X}_I}} \Big(w(|\mathbf{X}_{IJ}|)\mathbf{x}_{IJ}^n \otimes \mathbf{x}_{IJ}^n V_J^0\Big). \tag{56}$$

In the next section, we shall show that the non-local mapping $\mathbf{f}_I(t_{n+\alpha}) \approx \mathbf{F}_I(t_{n+\alpha})\mathbf{F}_I(t_n)^{-1}$.

In subsequent constitutive update:

If $f_{n+1}^{\mathrm{tr}} < 0$, elastic phase: update $\boldsymbol{\tau}_{n+1} = \boldsymbol{\tau}_{n+1}^{\mathrm{tr}}$ and $\mathbf{q}_{n+1}^{\zeta} = \mathbf{q}_n^{\zeta}$.

If $f_{n+1}^{\mathrm{tr}} \ge 0$, plastic phase:

$$\Delta\gamma = \frac{f_{n+1}^{\mathrm{tr}}}{2\mu + KB(\phi')B(\psi') + H^c(A(\phi'))^2}; \tag{57}$$

$$\boldsymbol{\tau}_I(t_{n+1}) = \boldsymbol{\tau}_I^{\mathrm{tr}}(t_{n+1}) - \Delta\gamma(KB(\psi'))\mathbf{I} + 2\mu\hat{\mathbf{n}}_I(t_{n+1}); \tag{58}$$

$$\mathbf{q}_I^{\zeta}(t_{n+1}) = \mathbf{q}_I^{\zeta}(t_n) + \Delta\gamma\mathbf{H} \cdot \mathbf{h}_I(\boldsymbol{\tau}, \mathbf{q}^{\zeta}). \tag{59}$$

3.2. Drucker–Prager plasticity model (cap model)

The yield and plastic potential functions f and g for the non-associative Drucker–Prager cap plasticity model are defined as

$$f\left(\boldsymbol{\tau}, \mathbf{q}^{\zeta}\right) = \|\mathbf{s}\| - \sqrt{F^{\phi}_{\text{cap}}}\sqrt{\left(A^{\phi} - B^{\phi} p\right)^2 - \left(A^{\phi} - B^{\phi}\zeta\right)^2} \tag{60}$$

$$A^{\phi} = \frac{2\sqrt{6}c\cos\phi}{3+\beta\sin\phi}; \quad B^{\phi} = \frac{2\sqrt{6}\sin\phi}{3+\beta\sin\phi}, \quad -1 \le \beta \le 1 \tag{61}$$

$$F^{\phi}_{\text{cap}} = 1 - H(\kappa - I_1)\left(\frac{I_1 - \kappa}{X^{\phi}(\kappa) - \kappa}\right)^2, \ \ 0 \le F^{\phi}_{\text{cap}} \le 1 \tag{62}$$

$$X^{\phi}(\kappa) = \kappa - R(A^{\phi} - B^{\phi}\kappa) \tag{63}$$

$$g\left(\boldsymbol{\tau}, \mathbf{q}^{\zeta}\right) = \|\mathbf{s}\| - \sqrt{F^{\psi}_{\text{cap}}}\sqrt{\left(A^{\psi} - B^{\psi} p\right)^2 - \left(A^{\psi} - B^{\psi}\zeta\right)^2} \tag{64}$$

where $\boldsymbol{\tau}$ is the Kirchhoff stress tensor, $\mathbf{s} := \boldsymbol{\tau} - (\tau_{mm}/3)\mathbf{I}$ is the deviatoric Kirchhoff stress, ϕ is the friction angle, and ψ denotes the dilatation angle. $\beta = -1$ indicates the Drucker–Prager yield surface passes through the triaxial compression vertices of the Mohr–Coulomb yield surface, while $\beta = 1$ indicating passing through the triaxial extension vertices of the Mohr–Coulomb yield surface. $\mathbf{q}^{\zeta}$ is the stress-like internal state variable associated with tension cap softening, κ is a parameter associated with compression cap position, and c is the constant cohesion. F^{ϕ}_{cap} is the yield cap function; R is the ellipticity of the compression cap; $H(\kappa - I_1)$ is the Heaviside function; $X^{\phi}(\kappa)$ denotes the position of the compression cap, whereas ζ denotes the position of the tension cap. Functional forms of F^{ψ}_{cap}, A^{ψ} and B^{ψ} are of the same form with F^{ϕ}_{cap}, A^{ϕ} and B^{ϕ}, respectively, except that ϕ is replaced with ψ.

For the Drucker–Prager cap model, the internal state variable (ISV) vector is $\mathbf{q}^{\zeta} = \{c, \phi, \psi, \zeta\}^T$, and the ISVs are evolving based on the following hardening/softening model,

$$\mathbf{H} = \begin{bmatrix} H^c & 0 & 0 & 0 \\ 0 & H^{\phi} & 0 & 0 \\ 0 & 0 & H^{\psi} & 0 \\ 0 & 0 & 0 & H^{\zeta} \end{bmatrix}, \tag{65}$$

where $H^c, H^{\phi}, H^{\psi}, H^{\zeta}$ are the linear hardening/softening moduli for c, ϕ, ψ, ζ, respectively.

The Kuhn–Tucker condition of plastic loading requires

$$f \le 0; \quad \dot{\gamma} \ge 0; \quad f\dot{\gamma} = 0. \tag{66}$$

During plastic loading, by using the consistency condition $\dot{f} = 0$, the plastic multiplier $\dot{\gamma}$ can be obtained as

$$\dot{\gamma} = \frac{\frac{\partial f}{\partial \boldsymbol{\tau}} : \mathbf{a} : \mathbf{d}}{\frac{\partial f}{\partial \boldsymbol{\tau}} : \mathbf{a} : \frac{\partial g}{\partial \boldsymbol{\tau}} - \frac{\partial f}{\partial \mathbf{q}^{\zeta}} : \mathbf{H} \cdot \mathbf{h}}. \tag{67}$$

The return-mapping algorithm involves the updating of the stress and stress-like ISVs at step n ($\boldsymbol{\tau}_n, \mathbf{q}^{\zeta}_n, \dot{\gamma}_n$) to those at step $n+1$ ($\boldsymbol{\tau}_{n+1}, \mathbf{q}^{\zeta}_{n+1}, \dot{\gamma}_{n+1}$), by making use of these coupled equations. The following is a standard return-mapping algorithm:

1. Update the stress tensor: Compute trial elastic stresses and evaluate the yield function

$$\boldsymbol{\tau}^{\text{tr}}_I(t_{n+1}) = \boldsymbol{\tau}_I(t_n) + \Delta\boldsymbol{\tau}_I \tag{68}$$

$$\left(\mathbf{q}^{\text{tr}}\right)^{\zeta}_I(t_{n+1}) = \mathbf{q}^{\zeta}_I(t_n) \tag{69}$$

$$f^{\text{tr}}_{n+1} = \|\mathbf{s}^{\text{tr}}_{n+1}\| - \sqrt{\left(F^{\phi}_{\text{cap}}\right)^{\text{tr}}_{n+1}}\sqrt{\left(A^{\phi} - B^{\phi}p^{\text{tr}}_{n+1}\right)^2 - \left(A^{\phi} - B^{\phi}\zeta_n\right)^2}. \tag{70}$$

2. Check for yielding:
   if $f^{\text{tr}}_{n+1} < 0$ (elastic phase),
   update the stress and the internal state variables (ISVs) as $\boldsymbol{\tau}_I(t_{n+1}) = \boldsymbol{\tau}^{\text{tr}}_I(t_{n+1})$; $\mathbf{q}^{\zeta}_I(t_{n+1}) = \mathbf{q}^{\zeta}_I(t_n)$
   else (plastic phase),
   solve $f(\Delta\gamma) = 0$ for $\Delta\gamma$ (consistency) and update the stress and ISVs correspondingly, and

3. Update the force state: $\mathbf{P}_I(t_{n+1}) = \boldsymbol{\tau}_I(t_{n+1})\mathbf{F}_I^{-T}(t_{n+1})$

$$\rightarrow \quad \underline{\mathbf{T}}^{IJ}[\mathbf{X}_I, t_{n+1}]\langle \mathbf{X}_{IJ}\rangle = \omega(|\mathbf{X}_{IJ}|)\mathbf{P}_I(t_{n+1})\mathbf{K}_I^{-1}\mathbf{X}_{IJ}.$$

In this work, no consistent tangent moduli is needed, because we are conducting explicit dynamic computations. For the sake of clarity and completeness, details of the algorithm in computing $\Delta\gamma$ for the Drucker–Prager cap model is provided in the Appendix A.

3.3. The Arenisca geomaterial model

To take into account the viscoplastic effect, porosity and saturated void effect, and soil grain disaggregation effect under blast loading, Brannon and her co-workers [25,26] have developed a semi-empirical geomaterial constitutive model to model the soil behaviors during explosions. This geomechanics model is named as Arenisca. The Arenisca soil model is a computational constitutive model for saturated or unsaturated sandstone in high-rate loading [44].

Since the Arenisca soil model is a semi-empirical constitutive model, it is carefully fitted with experimental data that are measured and obtained from the experiment of real geomaterials. From this perspective, it is a data-enhanced or data-driven constitutive model. The Arenisca model can take into account the viscoplastic effect of soil by using an overstress model. The Arenisca model has at least three different versions i.e. Arenisca 2.0, 3.0, and 4.0. In the following, we briefly outlined a simplified version of Arenisca 3.0 model, and it is the one used in the present study [45,46].

The plastic yield surface of the Arenisca model is a two function equation comprised of one that controls the shear behavior (F_f) and the other one that characterizing an elliptical cap (F_c) that controls the compressive behavior.

$$f = \sqrt{J_2} - \begin{cases} F_f(I_1) & ;\ I_1 \geq \kappa \\ F_f(I_1)F_c(I_1, X) & ;\ I_1 < \kappa \end{cases} \tag{71}$$

where J_2 is the second invariant of the deviatoric stress tensor, I_1 is the first invariant of the Cauchy stress, and κ and X are interdependent variables that control the location of the cap.

The Arenisca soil model adopts the following nonlinear form of the shear limits function

$$F_f = A_1 - A_3 e^{A_2 I_1} - A_4 I_1 \tag{72}$$

where A_1, A_2, A_3 and A_4 are material parameters. For simplicity, a linear Drucker–Prager shear limit function is used in the Arenisca model. F_f is a linear function

$$F_f = \beta(I_1^{\max} - I_1) \tag{73}$$

where β is the tangent of the friction angle (ϕ), and $I_1^{\max}$ is the tensile limit of the first stress invariant. One can see that for the linear case, $A_1 = \beta I_1^{\max}$, $A_3 = 0$ and $A_4 = \beta$.

The elliptical cap function F_c is defined as

$$F_c = \begin{cases} 1 & ;\ I_1 \geq \kappa \\ \sqrt{1 - \left(\dfrac{\kappa - I_1}{\kappa - X}\right)^2} & ;\ I_1 < \kappa, \end{cases} \tag{74}$$

where X is the intersection of the cap with the hydrostatic axis and κ is the isotropic hardening internal state variable that controls the location of the cap. A shape parameter (C_R) is used to control the geometry of the yield surface and it is assumed that during yielding, the yield surface geometry remains constant. In Arenisca 3.0, C_R is defined as

$$C_R = \frac{I_1^{\max} - \kappa}{I_1^{\max} - X}. \tag{75}$$

Evolution of κ is controlled by an empirical "crush curve" that is fitted to hydrostatic compression data in which the strains are measured in the experiment until a complete collapse of pore space in the soil. The curve is defined as

$$\epsilon_v^p = p_3\left(e^{-p_1(p_0 - X)} - 1\right), \tag{76}$$

where ϵ_v^p is the volumetric plastic strain; p_0 is three times the mean pressure at the elastic limit; p_1 is proportional to the initial slope of the porosity vs. pressure curve, and p_3 is the maximum plastic volumetric strain. For tensile response, the Arenisca soil model uses a hyperbolic function to describe the position of the cap with volumetric plastic strain, which is combined with the compressive crush curve to create a piecewise function.

$$X = p_0(\epsilon_v^p + 1)^{\frac{1}{p_0 p_1 p_3}}. \tag{77}$$

Fundamentally, the Arenisca model is a data-enhanced computational framework of geomaterial models. First, the Arenisca model is in fact a curve fitting model. Many material relations and parameters of the model are fitted with experimental data of drained or partially saturated Mason sand under various loading condition. These include: tangent modulus-mean stress relation, effective mean stress-elastic volumetric strain relation, effective mean stress-volumetric plastic strain relation, saturation-plastic volumetric strain relation, saturation-volumetric strain relation, porosity-effective mean strain relation, and among some other parameters and relations. For the detailed curve fitting procedures, readers are referred to [24]. Second, even though it may have a yield surface resembling that of the cohesive-frictional materials, but the term "yield" is generalized to include a broader class of inelastic responses of geomaterials such as backstress, porosity, saturation, and pore collapse and crush, etc. The Arenisca model also includes a partially saturated solid module. For implementation of the Arenisca partial saturated solid model, readers are referred to [24].

Compared with some thermodynamics-based geomaterial models, e.g. Borja's model [47], the Arenisca soil model may lack of physics-based mathematical deduction or rigorous. Since the main objective of this work is the modeling and simulation of soil fragmentation in engineering scale, a data-enhanced computational model may be more suitable than a geoscience based material model. Furthermore, the main focus of this work is about Peridynamics-SPH modeling and simulation of soil fragmentation, we refer readers to consult references [45,46] for the detailed information on computational aspects of the Arenisca model, such as consistent bisection (CB) algorithm and transformed-space closest-point return (TSCPR) algorithm.

3.4. Objective time-stepping algorithm

Recently we have found that the discrete nonlocal Peridynamics computation may not satisfy the material frame-indifference requirement, which may result in erroneous numerical results, if the objectivity is not strictly enforced. This could happen in both kinematic update of a vector or a tensorial field as well as constitutive update of stress or strain field.

To enforce the objectivity requirement, we adopt and apply the Hughes–Winget incremental objectivity algorithm in both the kinematic update as well as the stress update of the Peridynamics integration. The objective time-stepping algorithm adopted in this work mainly follows that in [48].

In the following, we briefly outline the main procedure. The trial stress in Eq. (52) is obtained under the assumption of small deformation. But in general, the soil particle under undergoes finite deformation with large rotations during blast loadings. To ensure an objective time integration, the Hughes–Winget algorithm [49] is implemented in the state-based Peridynamics framework. Between the two configurations at time step n and $n+1$, the Hughes–Winget algorithm introduces an intermediate configuration $n+\alpha$, such that the rate approximations of the spatial quantities (rate of deformation, stress tensor) are objective.

As shown in Fig. 7, an intermediate configuration at time step $n+\alpha$ is defined as

$$\mathbf{x}^{n+\alpha} := (1-\alpha)\mathbf{x}^n + \alpha\mathbf{x}^{n+1}, \quad 0 \le \alpha \le 1 \tag{78}$$

where α is a scalar. The nonlocal deformation gradient at the material point $\mathbf{X}_I$ in the configuration $\mathbf{x}_{n+\alpha}$ can be approximated as,

$$\mathbf{F}_I(t_{n+\alpha}) = \frac{\partial \mathbf{x}^{n+\alpha}}{\partial \mathbf{X}}\bigg|_{\mathbf{X}_I} := \left(\sum_{\mathbf{X}_J \in \mathcal{H}_{\mathbf{X}_I}} \omega(|\mathbf{X}_{IJ}|)(\mathbf{x}_J^{n+\alpha} - \mathbf{x}_I^{n+\alpha}) \otimes \mathbf{X}_{IJ} V_J^0\right) \cdot \mathbf{K}_I^{-1}, \tag{79}$$

which is a nonlocal strain measure.

In addition, the nonlocal gradient of displacement increment $\Delta\mathbf{u} = \mathbf{x}^{n+1} - \mathbf{x}^n$ with respect to the reference configuration can be formulated as,

$$\tilde{\nabla}_{\mathbf{X}} \Delta\mathbf{u}\bigg|_{\mathbf{X}_I} := \left(\sum_{\mathbf{X}_B \in \mathcal{H}_{\mathbf{X}_I}} \omega(|\mathbf{X}_{IJ}|)(\Delta\mathbf{u}_J - \Delta\mathbf{u}_I) \otimes \mathbf{X}_{IJ} V_J^0\right) \cdot \mathbf{K}_I^{-1}. \tag{80}$$

If this is a local gradient field, one can then obtain the increment of local deformation gradient via Chain Rule,

$$\mathbf{h}_{n+\alpha} = \frac{\partial(\Delta \mathbf{u})}{\partial \mathbf{x}_{n+\alpha}} = \tilde{\nabla}_{\mathbf{X}}(\Delta \mathbf{u}) \cdot \mathbf{F}^{-1}_{n+\alpha}. \tag{81}$$

However, the state-based Peridynamics is a nonlocal formulation of continuum mechanics, and one cannot directly apply Chain Rule in the above derivation. In the following, we shall show that Eq. (81) is valid for the non-local field as a first order approximation.

We first define $\mathbf{h}_{n+\alpha}$ at the material point I by considering the following updated Lagrangian derivative in the configuration $n+\alpha$,

$$\mathbf{h}_I(t_{n+\alpha}) := \left(\sum_{\mathbf{X}_J \in \mathcal{H}_{\mathbf{X}_I}} \omega(|\mathbf{X}_{IJ}|) \Delta \mathbf{u}_{IJ} \otimes \mathbf{x}^{n+\alpha}_{IJ} V^0_J \right) \cdot (\mathbf{K}^{n+\alpha}_I)^{-1}, \tag{82}$$

where

$$\mathbf{K}^{n+\alpha}_I := \sum_{\mathbf{X}_J \in \mathcal{H}_{\mathbf{X}_I}} \left(\omega(|\mathbf{X}_{IJ}|) \mathbf{x}^{n+\alpha}_{IJ} \otimes \mathbf{x}^{n+\alpha}_{IJ} V^0_J \right), \tag{83}$$

is the shape tensor in the configuration $n+\alpha$.

For a first order approximation, one can show that (see [27]),

$$\mathbf{F}_I(t_{n+\alpha}) := \mathbf{N}_I (\mathbf{K}^0_I)^{-1} \approx \mathbf{K}^{n+\alpha}_I \mathbf{N}^{-T}_I, \tag{84}$$

where

$$\mathbf{N}_I := \sum_{\mathbf{X}_J \in \mathcal{H}_{\mathbf{X}_I}} \left(\omega(|\mathbf{X}_{IJ}|) \mathbf{x}^{n+\alpha}_{IJ} \otimes \mathbf{X}_{IJ} V^0_J \right).$$

From Eq. (84), we have

$$\mathbf{K}^{n+\alpha}_I \approx \mathbf{F}_I(t_{n+\alpha}) \mathbf{N}^T_I \quad \rightarrow \quad (\mathbf{K}^{n+\alpha}_I)^{-1} \approx \mathbf{N}^{-T}_I (\mathbf{F}_I(t_{n+\alpha}))^{-1}, \tag{85}$$

and then one can show that

$$(\mathbf{F}_I(t_{n+\alpha}))^T (\mathbf{K}^{n+\alpha}_I)^{-1} = (\mathbf{K}^0_I)^T \mathbf{N}^T_I \cdot (\mathbf{N}^{-T}_I) \cdot (\mathbf{F}_I(t_{n+\alpha}))^{-1} = (\mathbf{K}^0_I)^T \cdot (\mathbf{F}_I(t_{n+\alpha}))^{-1}. \tag{86}$$

As mentioned in the previous section that in the state-based Peridynamics, the following relationship, i.e. the Cauchy–Born rule, is valid,

$$\mathbf{x}^{n+\alpha}_{IJ} \approx \mathbf{F}_I(t_{n+\alpha}) \cdot \mathbf{X}_{IJ}. \tag{87}$$

Substituting Eq. (87) into (82) and utilizing Eqs. (85) and (86), we have

$$\begin{aligned} \mathbf{h}_I(t_{n+\alpha}) &:= \frac{\partial(\Delta \mathbf{u})}{\partial \mathbf{x}_{n+\alpha}} \Big|_{\mathbf{X}_I} = \sum_{\mathbf{X}_J \in \mathcal{H}_{\mathbf{X}_I}} \left(\omega(|\mathbf{X}_{IJ}|) \Delta \mathbf{u}_{IJ} \otimes \mathbf{x}^{n+\alpha}_{IJ} V^0_J \right) \cdot (\mathbf{K}^{n+\alpha}_I)^{-1}, \\ &= \sum_{\mathbf{X}_J \in \mathcal{H}_{\mathbf{X}_I}} \left(\omega(|\mathbf{X}_{IJ}|) \Delta \mathbf{u}_{IJ} \otimes \mathbf{X}_{IJ} V^0_J \right) \cdot (\mathbf{F}_I(t_{n+\alpha}))^T (\mathbf{K}^{n+\alpha}_I)^{-1} \\ &= \sum_{\mathbf{X}_J \in \mathcal{H}_{\mathbf{X}_I}} \left(\omega(|\mathbf{X}_{IJ}|) \Delta \mathbf{u}_{IJ} \otimes \mathbf{X}_{IJ} V^0_J \right) (\mathbf{K}^0_I)^{-1} (\mathbf{F}_I(t_{n+\alpha}))^{-1} \\ &= \tilde{\nabla}_{\mathbf{X}} \Delta \mathbf{u} \cdot (\mathbf{F}_I(t_{n+\alpha}))^{-1}, \ \forall \alpha \in [0, 1] \end{aligned} \tag{88}$$

which is the nonlocal version of Eq. (81).

Eq. (88) can be split into the following strain and rotation increments,

$$\boldsymbol{\gamma}_I = (\mathbf{h}_I(t_{n+\alpha}) + \mathbf{h}^T_I(t_{n+\alpha}))/2, \tag{89}$$

$$\boldsymbol{\omega}_I = (\mathbf{h}_I(t_{n+\alpha}) - \mathbf{h}^T_I(t_{n+\alpha}))/2. \tag{90}$$

In passing, we note that both kinematic quantities are nonlocal. The objective effective stress increment is evaluated as,

$$\Delta\boldsymbol{\tau} = \mathbf{a} : \boldsymbol{\gamma}. \tag{91}$$

Finally, Eq. (52) is replaced by the following set of equations

$$\boldsymbol{\tau}_I^{\mathrm{tr}}(t_{n+1}) = \hat{\boldsymbol{\tau}}_I(t_n) + \mathbf{a}_I : \boldsymbol{\gamma}_I, \tag{92}$$

$$\hat{\boldsymbol{\tau}}_I(t_n) = \boldsymbol{\Lambda}_I^T \boldsymbol{\tau}_I(t_n) \boldsymbol{\Lambda}_I, \tag{93}$$

$$\boldsymbol{\Lambda}_I = \mathbf{I} + (\mathbf{I} - \alpha\boldsymbol{\omega}_I)^{-1}\boldsymbol{\omega}_I. \tag{94}$$

We now show that $\mathbf{f}_I(t_{n+\alpha}) = \mathbf{F}_I(t_{n+\alpha})(\mathbf{F}_I(t_n))^{-1}$.

Let $\alpha = 0$ in Eq. (88), we have

$$\begin{aligned} \tilde{\nabla}_x \Delta\mathbf{u}_I &= \tilde{\nabla}_X \Delta\mathbf{U}_I \cdot (\mathbf{F}_I(t_n))^{-1} \\ \to \quad \tilde{\nabla}_X \Delta\mathbf{U}_I &= \tilde{\nabla}_x \Delta\mathbf{u}_I \cdot \mathbf{F}_I(t_n), \ \forall \mathbf{X}_I \in \Omega_0. \end{aligned} \tag{95}$$

By definition,

$$\mathbf{F}_I(t_{n+\alpha}) = \mathbf{F}_I(t_n) + \alpha(\mathbf{F}_I(t_{n+1}) - \mathbf{F}_I(t_n)) = \mathbf{F}_I(t_n) + \alpha\tilde{\nabla}_X \Delta\mathbf{U}_I.$$

Substituting Eq. (95) into the above equation yields

$$\begin{aligned} \mathbf{F}_I(t_{n+\alpha}) &= \mathbf{F}_I(t_n) + \alpha\tilde{\nabla}_X \Delta\mathbf{U}_I = \mathbf{F}_I(t_n) + \alpha\tilde{\nabla}_x \Delta\mathbf{u}_I \cdot \mathbf{F}_I(t_n) \\ &= \mathbf{I} + \alpha\tilde{\nabla}_x \Delta\mathbf{u}_I \mathbf{F}_I(t_n). \end{aligned}$$

We then have the desired result,

$$\mathbf{f}_I(t_{n+\alpha}) := \mathbf{I} + \alpha\tilde{\nabla}_x \Delta\mathbf{u}_I = \mathbf{F}_I(t_{n+\alpha}) \cdot (\mathbf{F}_I(t_n))^{-1}, \tag{96}$$

which is what we have used in the simulations. In passing, we note that the desired objectivity result (96) requires the nonlocal formulation converges to the local formulation, i.e. Eq. (84) (see [27]). If a nonlocal method does not mathematically converge to an objective local formulation, the above proof will be not valid; and we know that some nonlocal particle material models do not converge to the localized Cauchy continuum in terms of rigorous mathematical arguments, whose objectivity issue is still an open problem. Numerical study on the objectivity of the time-stepping algorithm is discussed in the following section.

4. Numerical examples

In this section, several numerical examples are presented. First, a three-dimensional column is prescribed with uniaxial compression, to verify the Peridynamics model and the corresponding numerical implementation. Second, two numerical tests are conducted to demonstrate the objectivity of the time integration algorithm for the Drucker–Prager cap plasticity model. Finally, the PD-SPH coupling method is employed to simulate soil fragmentation under blast loading for three different soil constitutive models.

4.1. A three-dimensional soil column under uniform step load

Fig. 3(a) shows the geometrical configuration of a soil column with a square cross-section of side length $L = 1$ m and height $H = 10$ m. The soil column is uniformly discretized into 14,196 Peridynamics particles. A pressure load $P(t)$ is applied at the top surface. The step load $P(t)$ is shown in Fig. 4, with the maximum pressure P_0 and rising time t_0. The bottom of the soil column is fixed in the vertical (z) direction and the four side surfaces are confined with zero displacements in the corresponding out-normal directions, in order to produce a one-dimensional loading condition. The simulation time step is chosen to be $dt = 1.0 \times 10^{-3}$ s, with a total simulation time $t = 2.0$ s. The material parameters of all three geomaterial models are provided in Table 2. The adaptive dynamic relaxation method for the Peridynamics (see [50]) is employed to obtain a steady-state solution in the dynamic simulation. Three different load cases with $P_0 = 10,\ 20,\ 30$ kPa and $t_0 = 0.05$ s are considered. The numerical results are compared to the small strain steady-state analytical solution of consolidated vertical displacement under small deformation (linear elastic).

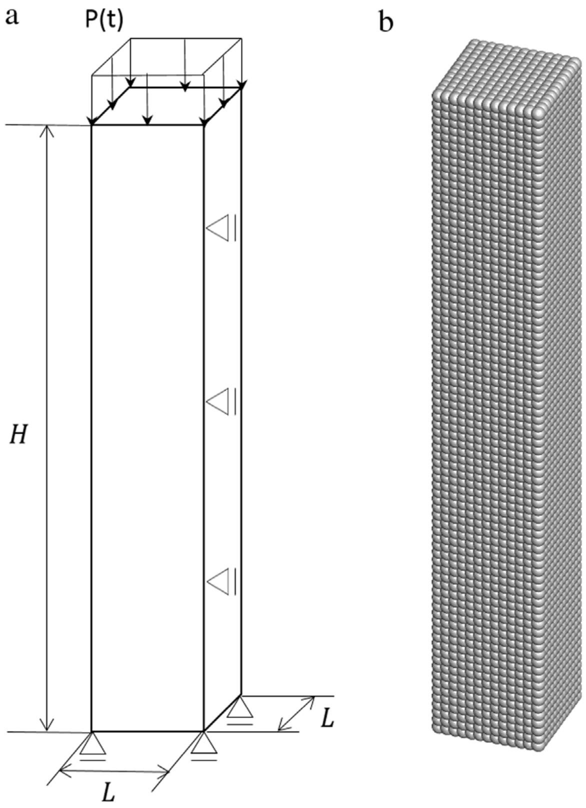

Fig. 3. A three-dimensional soil column under uniform step load: (a) geometrical configuration; (b) representation of the domain with 14,196 particles.

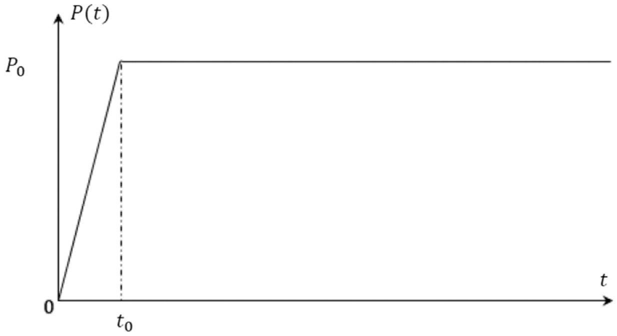

Fig. 4. A step loading function with maximum value P_0 and rising time t_0.

The analytical solution for the vertical displacement at the top of the column is $\Delta H = (P_0 H)/(\lambda + 2\mu)$ [51], where λ and μ are the Lame constants. From the comparison in Fig. 5, one can see that the numerical results are in good agreement with the analytical solutions at the regime of small strain, which to some extent proves the validity of the implementation of the Peridynamics model.

4.2. *Objectivity of the time-stepping algorithm*

To validate the Peridynamics numerical integration algorithm for finite deformation, we first test its objectivity in the sense of frame-indifference [52].

Table 2
Material parameters used in the computation for three geomaterial models.

Drucker–Prager	E	μ	H^c	ϕ	ψ	β				
(uncapped)	98.5 (MPa)	0.25	0.2 (MPa)	0.74	0.74	−1				
Drucker-Prager	E	μ	R	κ	H^χ	H^c	ϕ	ψ	c_0	β
(capped)	98.5 (MPa)	0.25	10	−2 (KPa)	−100 (MPa)	0	0.35	0.17 (KPa)	100	−1
	E	μ	β	$I_1^{\max}$	C_R	P_0	P_1	P_2		
Arenisca model	98.5 (MPa)	0.25	0.65	1	0.5	−0.33	1.2e−8	0.25		

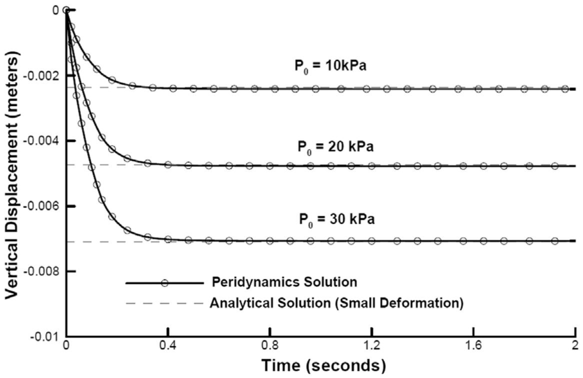

Fig. 5. Convergence of the nonlocal Peridynamics solutions to the analytical solutions.

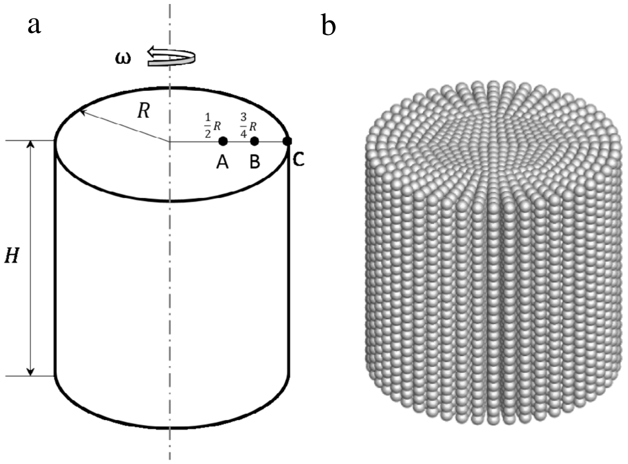

Fig. 6. A soil cylinder: (a) geometrical configuration; A, B and C are particles on the top surface; (b) representation of the cylinder with 11,882 particles.

4.2.1. *A solid cylinder with rigid-body rotation*

Fig. 6 shows the configuration of a cylinder with a radius $R = 0.025$ m and height $H = 0.05$ m. Particle A, B and C are located at the top surface of the cylinder with the distances to the principle axis $r_A = 1/2R$, $r_B = 3/4R$ and $r_C = R$. The cylinder is prescribed with an initial angular velocity $\omega = 1000$ rad/s, with respect to the principal axis. Subjected to no external displacement or traction boundary conditions, the cylinder is expected to continuously rotate with initial angular velocity ω forever (rigid body motion with no deformation). The material properties of

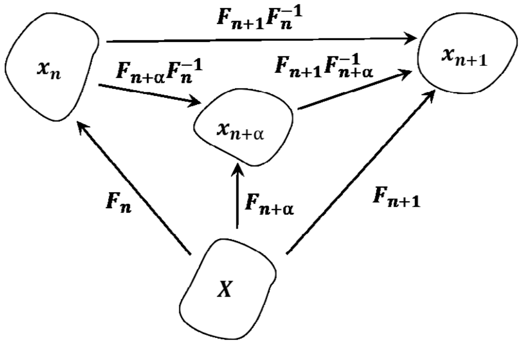

Fig. 7. Geometric relations of the intermediate configuration $\mathbf{x}_{n+\alpha}$.

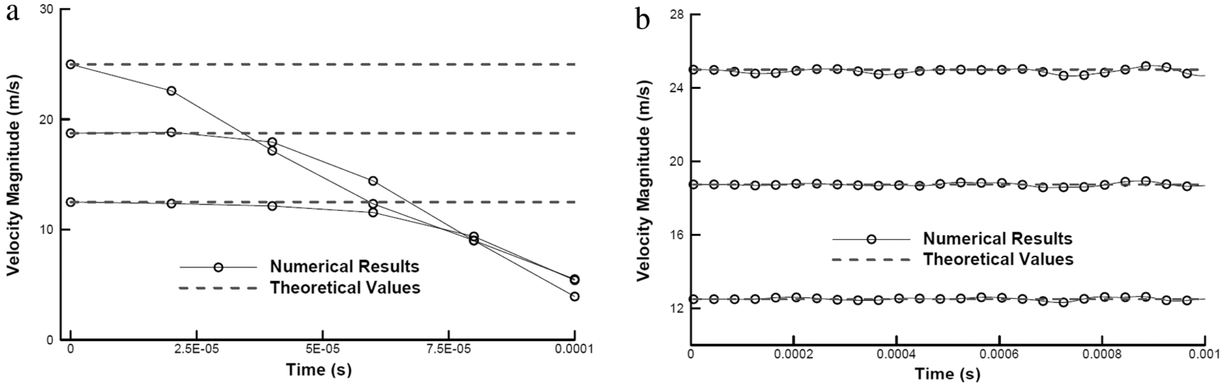

Fig. 8. Comparison of numerical and analytical results for velocity magnitudes at specific positions: (a) without the objective time-stepping algorithm; (b) with the objective algorithm.

the soil are shown in Table 2. The time step is set to be $dt = 5.0 \times 10^{-7}$ s, in order to comply with the Courant–Friedrichs–Lewy (CFL) condition [53]. The total simulation time is $t = 1.0 \times 10^{-3}$ s. To check the objectivity of the proposed time-stepping algorithm, the velocity magnitudes of the three particles A, B and C are recorded and plotted against the simulation time. Fig. 8(a) shows the numerical results of particle velocity magnitudes for the case without the objective time-stepping algorithm, all of which diverge from the theoretical values $v_A = \omega r_A = 12.5$ m/s, $v_B = 18.75$ m/s and $v_C = 25$ m/s, for only a few time steps. On the contrary, the numerical results of the velocity magnitudes obtained with the objective time-stepping algorithm compare quite well with the theoretical values, as shown in Fig. 8(b). In fact, they simply oscillate around the theoretical values, owing to the inertial effects. From this example, one can see that the proposed integration algorithm in the framework of the state-based Peridynamics is invariant or incrementally invariant under the rigid body rotations. Instead of producing non-physical deformations in the soil cylinder, the algorithm passed the benchmark test, and it provides physically correct results. In other words, it satisfies the objectivity requirement.

4.2.2. *A three-dimensional column under harmonic loading*

To take a further look at the objectivity of the algorithm, a numerical example with the presence of both loading and initial rotation is presented. Fig. 9 shows a soil column with side length $L = 1$ m and height $H = 10$ m. The soil column is uniformly discretized into 6804 particles. A harmonic pressure load $P(t)$ (see Fig. 10) is applied at the top surface. The bottom surface is fixed in the vertical direction and the four side surfaces are free. The material parameters are shown in Table 2. The simulation time step is set to be $dt = 5.0 \times 10^{-4}$ s, with the total simulation time $t = 1.5$ s. The maximum loading pressure is $P_0 = 40$ kPa and the initial angular velocity (with respect to the principal axis of the column) is $\omega = 1.57$ rad/s. The analytical solution for the vertical displacement at the top surface

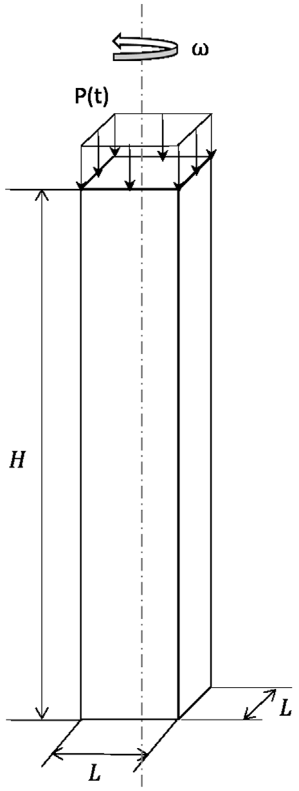

Fig. 9. A schematic of a soil column with initial angular velocity ω subjected to a pressure load $P(t)$ at the top surface.

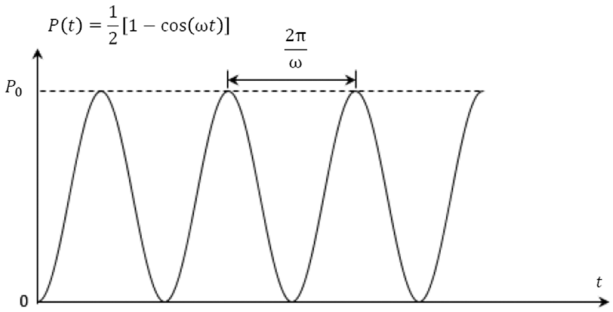

Fig. 10. A harmonic loading function with maximum load P_0.

of the column (under small deformation) is

$$\Delta H = \frac{P_0 H}{2E}\left[1 + \frac{(\omega/\omega_n)^2}{1-(\omega/\omega_n)^2}\cos\omega_n t - \frac{1}{1-(\omega/\omega_n)^2}\cos\omega t\right], \tag{97}$$

where E is the Young's modulus and ω_n is the natural frequency. Subjected to the harmonic pressure loading at the top surface, numerical tests with and without the presence of rotation around the axis are conducted. Fig. 11(a) shows the comparison of the top surface displacements for the case without objective time-stepping algorithm, together with the analytical solution. One can see that with the presence of rigid body rotation, the simulation results diverge from the theoretical value for merely a few time steps. On the contrary, Fig. 11(b) shows that the top surface displacements obtained with the proposed objective time-stepping algorithm. It can be seen that the rotation has little effect on the results, although with the presence of the loading, which further proves the objectivity of the proposed algorithm. For

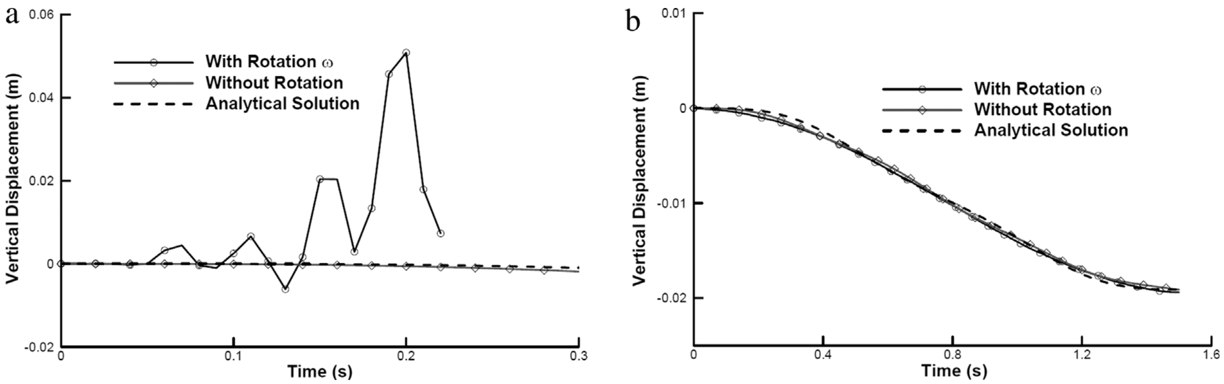

Fig. 11. Comparison of numerical and analytical results for vertical displacements at the top of the column: (a) without the objective time-stepping algorithm; (b) with the objective algorithm.

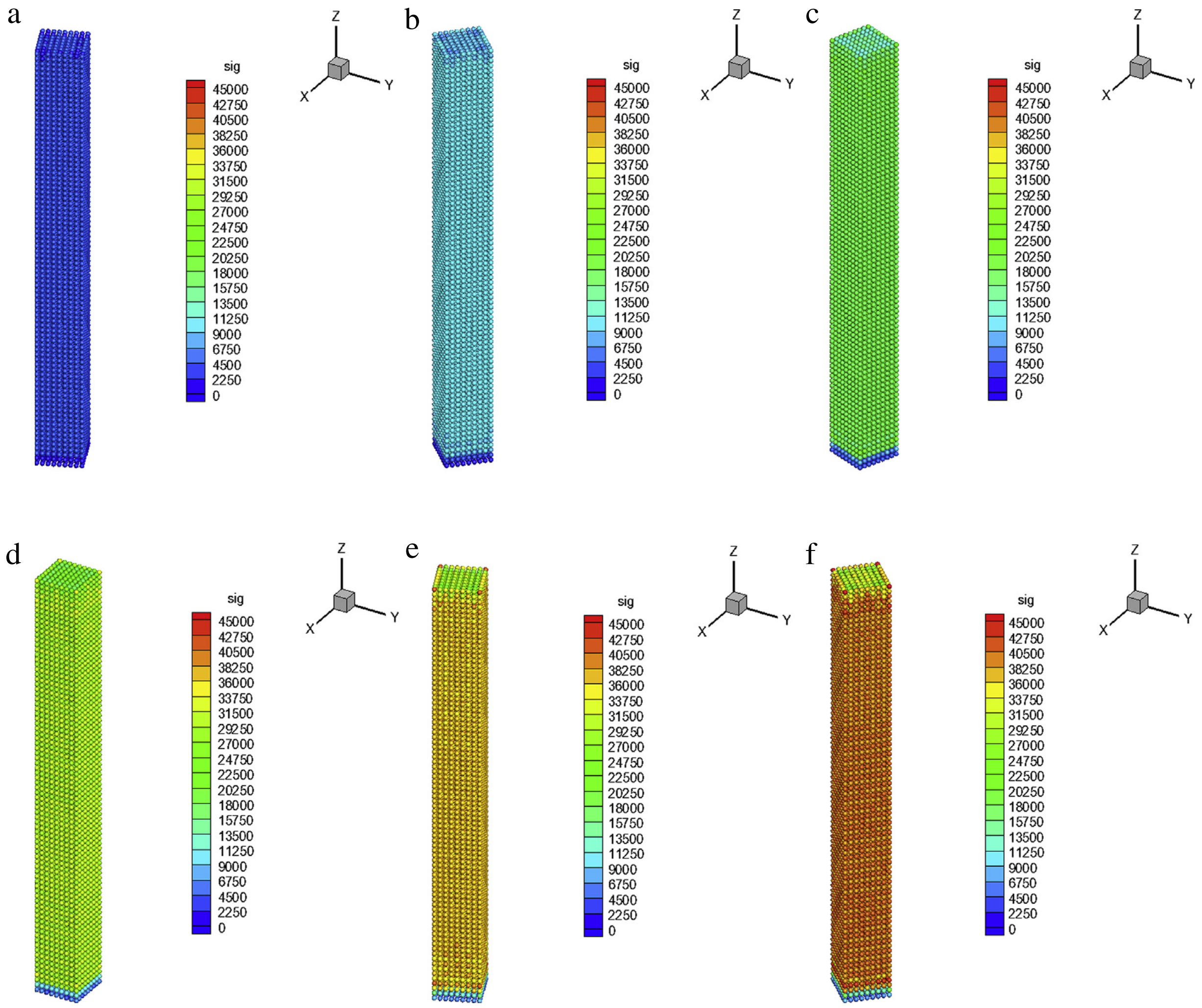

Fig. 12. Effective stress distribution during the compressing/rotating process.

the sake of completeness, a time sequence of the column during the compressing/rotating process (simulated with the objective integration algorithm) is shown in Fig. 12.

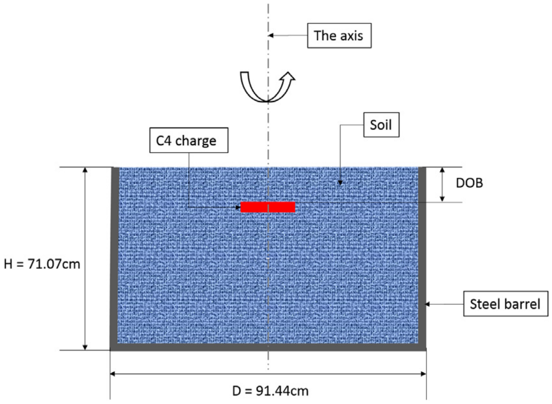

Fig. 13. A schematic of the experiment setup used in [43].

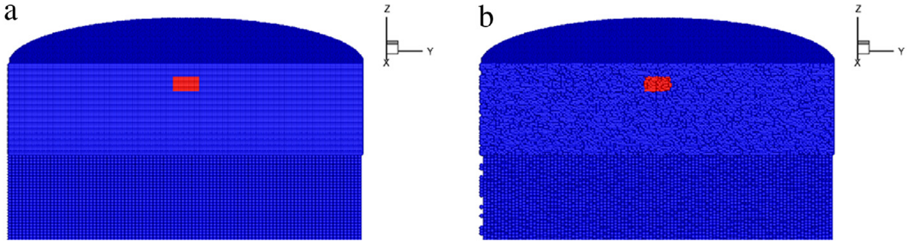

Fig. 14. Representation of the computational domain with 4,891,414 Peridynamics particles (blue) and 2477 SPH particles (red): (a) Uniform particle distribution, and (b) Random particle distribution. (For interpretation of the references to color in this figure legend, the reader is referred to the web version of this article.)

4.3. Explosive induced soil fragmentation

In this example, the PD-SPH coupling method is employed to simulate the soil fragmentation resulting from detonation of 100-gram charge of C4 explosive. Fig. 13 shows the simulation setup, which is exactly the same as the experiments conducted by Bergeron et al. [43]. A cylindrical barrel with the radius of 45.72 cm and the height of 71.07 cm is fully filled with soil. A 100-gram C4 explosive charge of cylindrical-disk shape is buried into the soil along the axis of the barrel with its face parallel to the soil surface. The distance between the top face of the explosive and the soil surface is defined as the depth of burial (DOB). Two different overburdens with DOBs 3 cm and 8 cm are considered in the simulation.

To reduce the computational cost, a semi-uniform discretization of the computational domain is adopted. The whole domain is divided into two different regions, each of which is discretized uniformly with a unique particle space $\varDelta_i$, $i = 1, 2$. Given that we are mainly interested in the soil deformation around the explosive charge, the region embedded with the C4 charge is discretized with the smallest particle space $\varDelta_1 = 4.0 \times 10^{-3}$ m, whereas the other region is discretized with $\varDelta_2 = 2\varDelta_1$. As shown in Fig. 14(a), the whole domain contains 4893,891 particles, of which 4,891,414 are Peridynamics (soil) particles and 2477 are SPH (C4 charge explosive) particles. To check whether the simulation result is sensitive to the initial particle distributions or not, an additional particle distribution is generated from a random perturbation of the semi-uniform discretization (see Fig. 14(b)). In particular, the particle position $\mathbf{X}'$ of an old particle $\mathbf{X}$ in the new discretization is obtained through the following formula,

$$\mathbf{X}' = \mathbf{X} + 0.05\mathbf{rand}\varDelta_i, \tag{98}$$

where $\mathbf{X}$ is the particle position in the semi-uniform discretization, **rand** is a random vector with each component $-0.5 \leq rand(j) \leq 0.5$, $j = 1, 3$ and $\varDelta_i$ is the smallest particle space in the corresponding region. The statistical distribution of the random number is the Gaussian distribution.

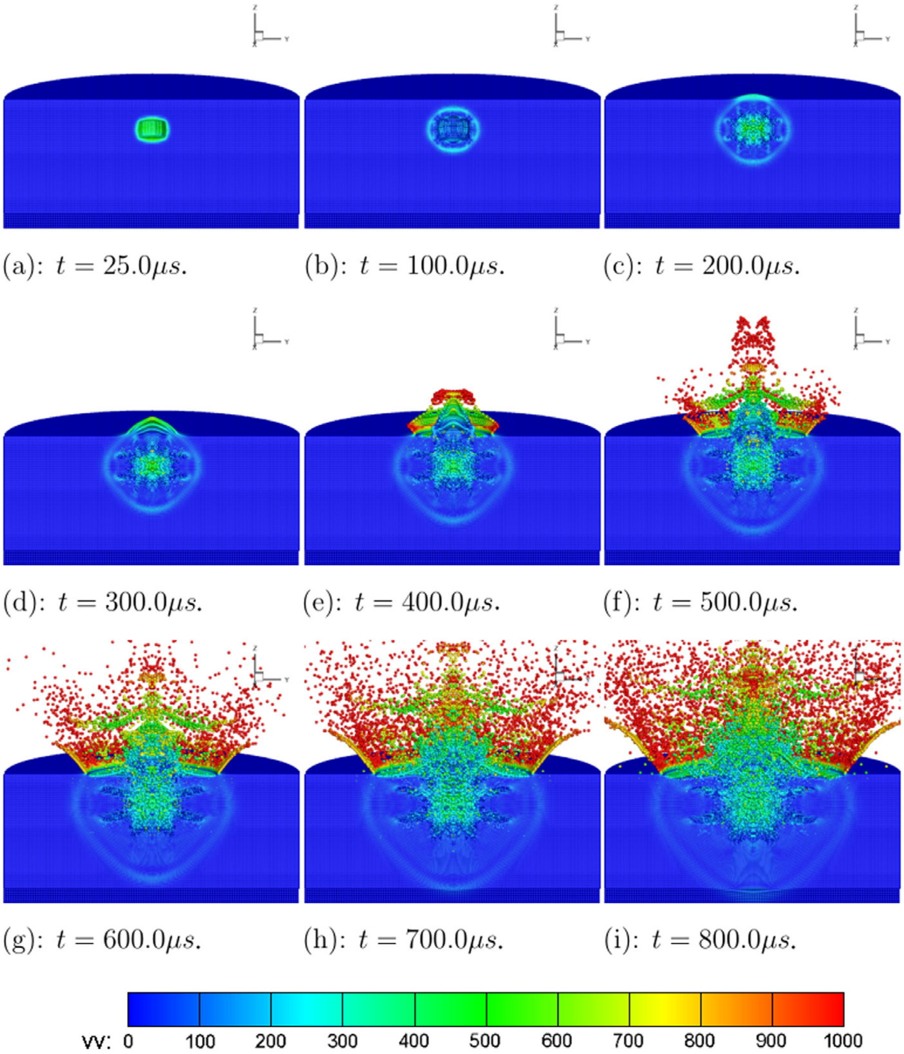

Fig. 15. Time sequence of the dynamic soil fragmentation process for uncapped Drucker–Prager model: DOB = 8 cm, non-perturbed semi-uniform discretization; The contour color represents the velocity magnitude (m/s). (For interpretation of the references to color in this figure legend, the reader is referred to the web version of this article.)

The Jones–Wilkins–Lee (JWL) equation of state is used to model the C4 explosive charge. The parameters for the C4 charge are taken from [38]. The simulation time step is chosen to be $\Delta t = 0.25 \times 10^{-6}$ s, with the total time $t = 0.8 \times 10^{-3}$ s. A parallel PD-SPH code is developed by using the OpenMP [54] application program interface. By using the PD-SPH coupling method, computer simulations of a system of total 4,891,414 material particles are carried out by using 16 and 32 threads, respectively, in the same Intel(R) Xeon(R) E5-2698 CPU. The total simulation time recorded for the 16 threads case is around 77.5 h, the total simulation time recorded for the 32 threads case is around 42.0 h. For the detailed OpenMP implementation of PD-SPH method, the readers are referred to [55].

The time sequence of the dynamic soil fragmentation process for the overburden of DOB 8 cm is presented in Fig. 15, with the color contour denoting the velocity magnitude, with the unit of meter per second. From Fig. 15, one can see that the SPH particles gained very large momentums immediately after the ignition, resulting from the enormous energy of the explosive charge. The shock waves quickly propagated through the interaction zone of the SPH and Peridynamics particles (interphase zone), which indicates the coupling of the Peridynamics and SPH particles is successful. After passing through the interphase zone, the shock waves continuously expanded in each direction.

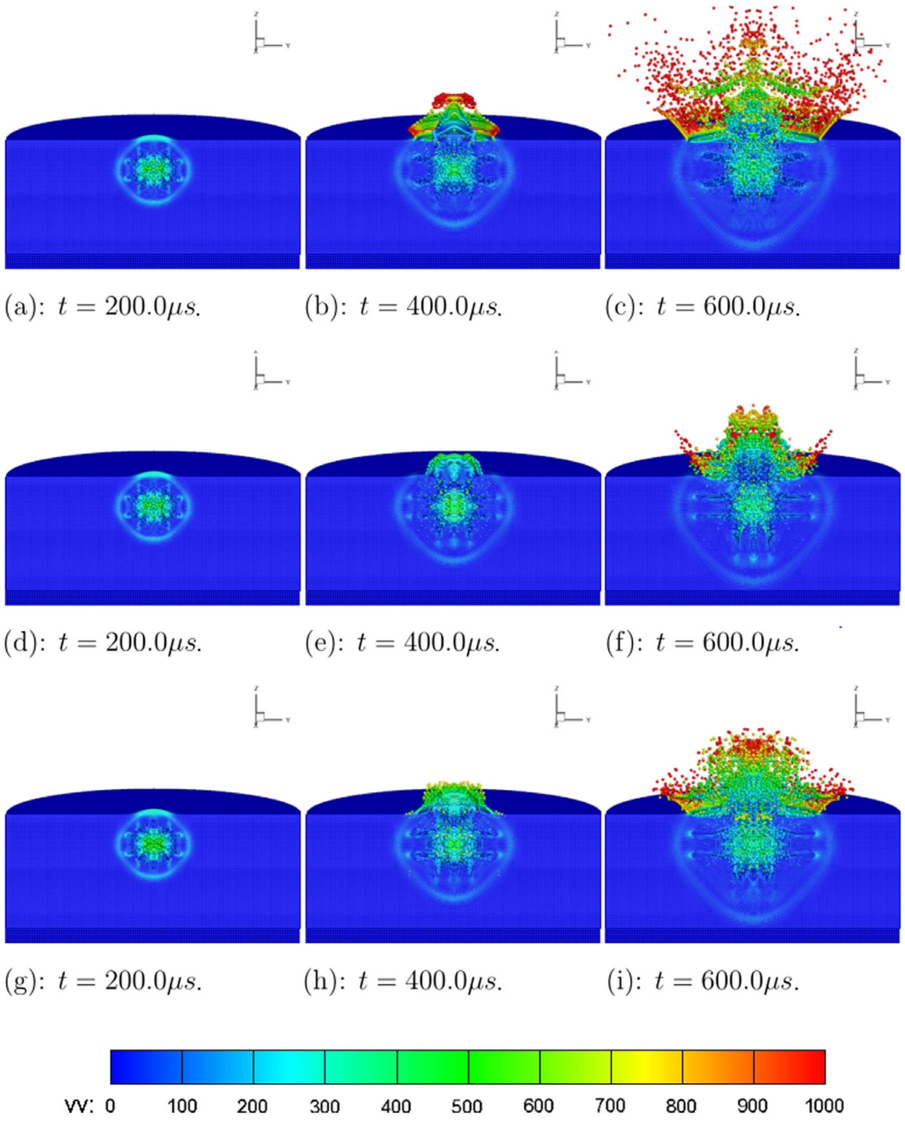
(a): $t = 200.0\mu s.$ (b): $t = 400.0\mu s.$ (c): $t = 600.0\mu s.$

(d): $t = 200.0\mu s.$ (e): $t = 400.0\mu s.$ (f): $t = 600.0\mu s.$

(g): $t = 200.0\mu s.$ (h): $t = 400.0\mu s.$ (i): $t = 600.0\mu s.$

Fig. 16. Comparison of the dynamic soil fragmentation process: DOB = 8 cm; Three different constitutive models; (a–c) for the uncapped Drucker–Prager model, (d–f) for the Drucker–Prager cap model and (g–i) for the Arenisca model. The contour color represents the velocity magnitude (m/s). (For interpretation of the references to color in this figure legend, the reader is referred to the web version of this article.)

When the first shock wave reached the top surface of the cylinder, a small soil bubble started to form (Fig. 15(b)), and it gradually grew in its height and width.

Fig. 16 shows comparisons between the simulation results obtained from three different soil constitutive relations. Overall, the soil fragmentation patterns are similar, but they differ in details. First one may find that the shock wave fronts of all three simulations are almost the same. This makes sense, because we used the same Young's modulus (98.5 MPa) and the Poison's ratio 0.25 for all three models (see Table 2). On the other hand, it seems to us that the uncapped Drucker–Prager model has less resistance to soil fragmentation than that of the Drucker–Prager cap model and the Arenisca model. Even though the results obtained by using the Drucker–Prager cap model and the Arenisca soil mode are similar, the soil bubble shapes obtained from these two different modeling methods have distinct differences in the tangential soil ejecta angle and overall profiles (see Fig. 16).

Fig. 14 is a comparison of numerical models ("meshes") between uniform particle distribution and non-uniform particle distribution, while Fig. 17 shows the comparison of dynamic soil fragmentation profiles between the two

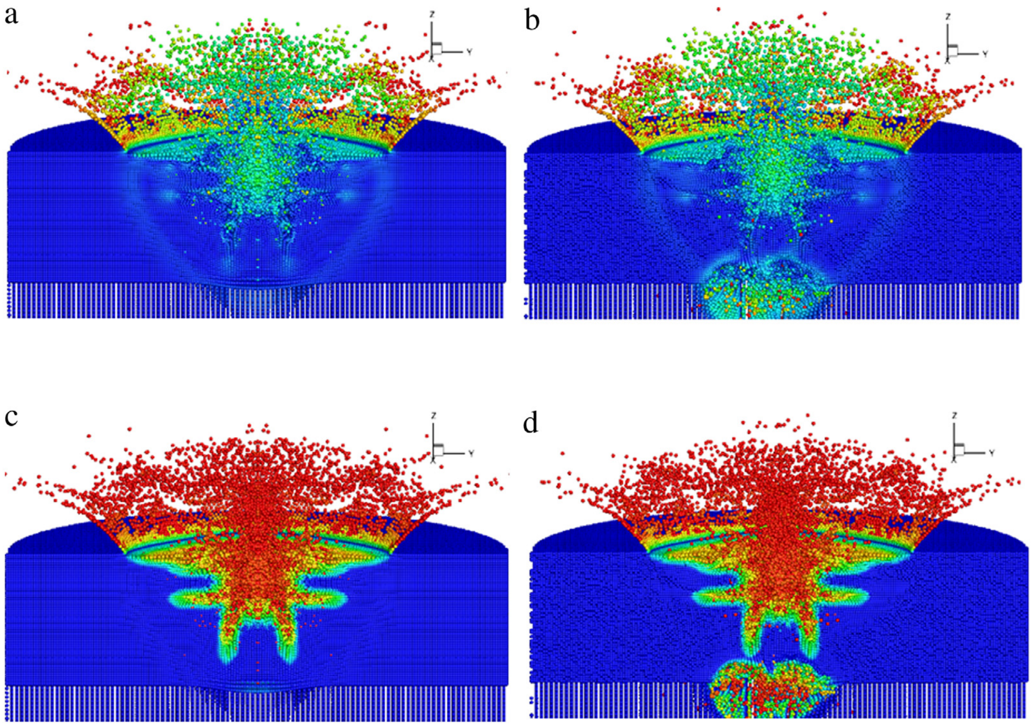

Fig. 17. Comparison of soil bubble fragmentation between uniform discretization model and non-uniform discretization model (DPC): (a) Velocity field and (c) Damage field for a uniform particle distribution model, and (b) Velocity field and (d) Damage field for a non-uniform particle distribution model.

models i.e. the uniform particle distribution and the non-uniform particle distribution. In Fig. 17(a) (b), the color contour is the magnitude of the velocity field in soil, and in Fig. 17(c) (d) the color contour is the magnitude of the damage field in soil. In both cases, the Drucker–Prager Cap (DPC) model is used in the simulation. The velocity and damages contours for both have similar patterns, except that for the case of the uniform particle distribution, those patterns are almost symmetric whereas for the case of non-uniform mesh both velocity field and damage field have certain asymmetric profiles. For the case of non-uniform particle distribution, those asymmetric patterns become prominent when the first shock wave arrives at the interface of two regions with different particle densities as shown in Fig. 17. This may attribute to the shock wave reflection and deflection at the inhomogeneous interface. The non-uniform particle distribution will also induce the non-uniform impedance at the interface, which may cause the asymmetric reflection at the interface. Nevertheless, we are mainly interested in the early stage of the soil fragmentation before the first shock wave hits the boundary region.

The early soil deformation and fragmentation state, i.e. the soil bubble shape as an ejecta front, obtained from the simulations are compared with that obtained from the experimental measurement, e.g. [43]. The time histories of the soil bubble height and width evolution of the ejecta front for both the 3 cm and 8 cm depth of burial (DOB) are plotted in Fig. 19(a)–(f) for three soil models, respectively. The definition for the width and height of a soil bubble is shown in Fig. 18. The curve of the bubble height for the 3 cm DOB, i.e. the first curve (blue) (3 cm–simulation) in Fig. 19(a), (c), and (e), are used to calibrate simulation parameters. The rest three sets of curves (8 cm for height and both curves for width) in Fig. 19 are obtained as the predictive values that are extracted from simulation results with the set of the parameters calibrated in the first case. One can see that the soil bubble height of the 8 cm DOB matches well with that of the experiment results for the Drucker–Prager cap model as well as the Arenisca model. The bubble widths obtained for simulations of both 3 cm and 8 cm DOBs are both in general agreement with the experimental data with small discrepancies ($<10\% \sim 20\%$), which may be attributed to the fact that the smallest particle gap ($\Delta_1 = 4.0 \times 10^{-3}$ m) is much larger than the typical sand size ($0.16 \sim 0.63 \times 10^{-3}$ m) in the experiment. However, both the uncapped Drucker–Prager model and the Arenisca model give good predictions on soil bubble width in the case of 3 cm DOB; whereas the Drucker–Prager cap model gives good prediction on soil bubble width in the case of 8 cm DOB.

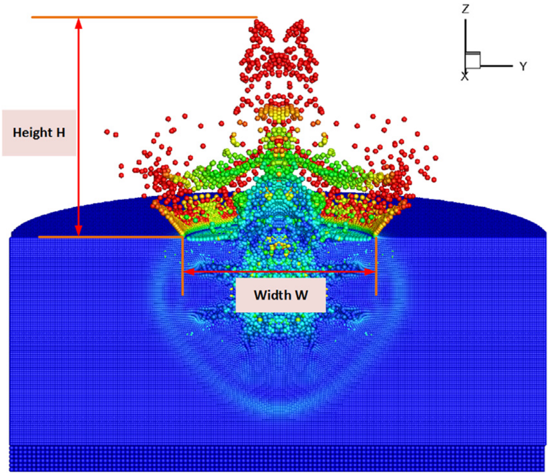

Fig. 18. Definitions of the width and height of a soil bubble.

The difference in the resolutions of the particle gaps inevitably introduces the difficulties in identifying the shapes, especially the widths of the early soil bubbles. Nevertheless, to a large extent, the simulation result validates the PD-SPH coupling method and its application in the modeling of soil fragmentation.

Moreover, the simulation results for the uncapped Drucker–Prager model show localized soil bubbles growing inside the exterior bubble and then collapsing at late stage. In Fig. 20, we show a sequence of soil bubble evolution obtained in a two-million particle simulation that uses the uncapped Drucker–Prager model as its soil constitutive model. It is worth noting that even though the uncapped Drucker–Prager model renders poor prediction on the soil bubble height, its related simulation results show a distinct soil bubble shape that contains explosive gas with outward expansion. Moreover, from Fig. 20, one may observe that there is a mixed soil/gas jet inside the soil bubble first, and then it is bursting out the outer layer of the soil bubble in the fragmentation stage of the event. To the best of the authors' knowledge, this phenomenon has never been reported before in open literature, and it is somewhat similar to gas bubble bursting out of the water in underwater explosions.

5. Discussions

It has been a technical challenge in several decades to accurately predict soil fragmentation caused by blast loadings. In this work, we present a Peridynamics/SPH coupling method in modeling and simulation of soil fragmentation caused by underground explosion of the buried explosive charge in an attempt to quantitatively predict laboratory scale soil fragmentation under blast loads.

In this work, we first used the experimental measurement data in the literature to tune the parameters in the Peridynamics model, and then used the Peridynamics model to predict a different set of experimental results. Remarkably, it has been found that the Peridynamics simulation results or the predictions on the new set of experiments are in general agreement with the experimental data.

Moreover, we have shown that (1) the proposed Peridynamics soil formulation with the non-local Hughes–Winget integration algorithm can pass the objectivity benchmark test; (2) the Peridynamics computation also works on unstructured random particle distribution, and (3) by using the OpenMP parallel algorithm we can conduct a large scale Peridynamics simulation (up to 5 million particles) in a desktop workstation. We would like to point out that even though the objective time-integration algorithm has been developed since 1980s, they have been mainly applied to the Galerkin weak formulation based finite element method in local continuum mechanics. To the best of the authors' knowledge, the present work may be the first case that the objective time-integration procedure is being applied to the nonlocal continuum mechanics based Peridynamics formulation, or the state-based Peridynamics.

Even though the Drucker–Prager models, both the uncapped and the capped, provide reasonable estimates to the soil behaviors such as strain localization under quasi-static loading, it may not be suitable for soil behaviors under high strain rate loadings. In this respect, the Arenisca model may provide some useful predictions, because it is a

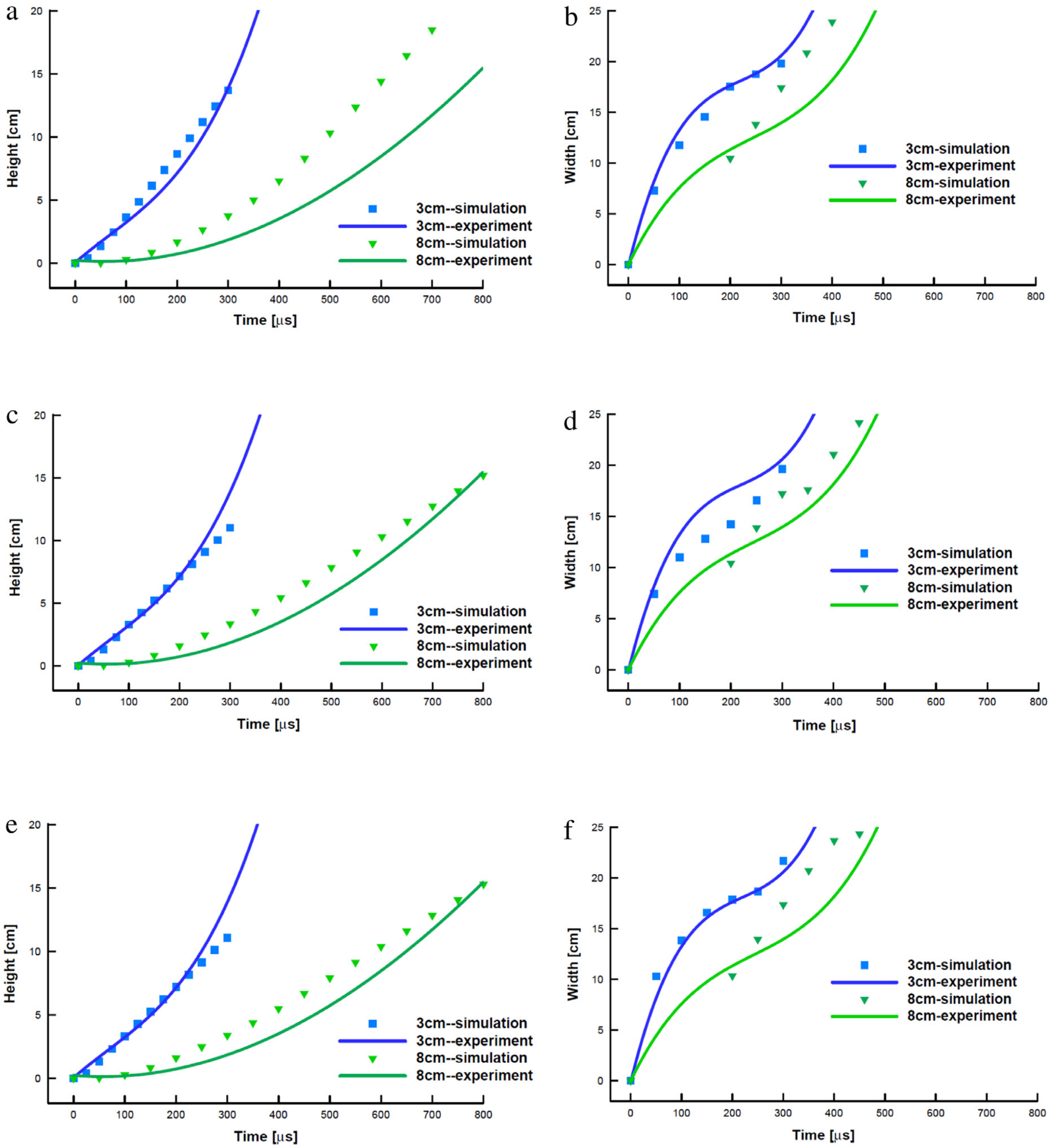

Fig. 19. Comparison of soil bubble shapes (height (a, c, e) and width (b, d, f)) at the soil ejecta front for both 3 cm and 8 cm overburdens with experimental results from [43]; (a–b) for the uncapped Drucker–Prager model; (c–d) for the Drucker–Prager cap model; (e–f) for the Arenisca Model.

data-enhanced constitutive model for high strain rate loading. However, one may argue that all these constitutive models discussed above may not correctly predict soil motion during or after soil fragmentation because after a soil medium fragments some soil particles no longer interact with each other. This is one of the motives of the present development of Peridynamics modeling. Fundamentally, the state-based Peridynamics soil model developed in this work is an advanced or complex “discrete element approach”, which models the soil particle as a soft sphere. The radius of the sphere is the radius of the horizon, δ_I, for particle I. (See Fig. 21). After fragmentation, a soil particle,

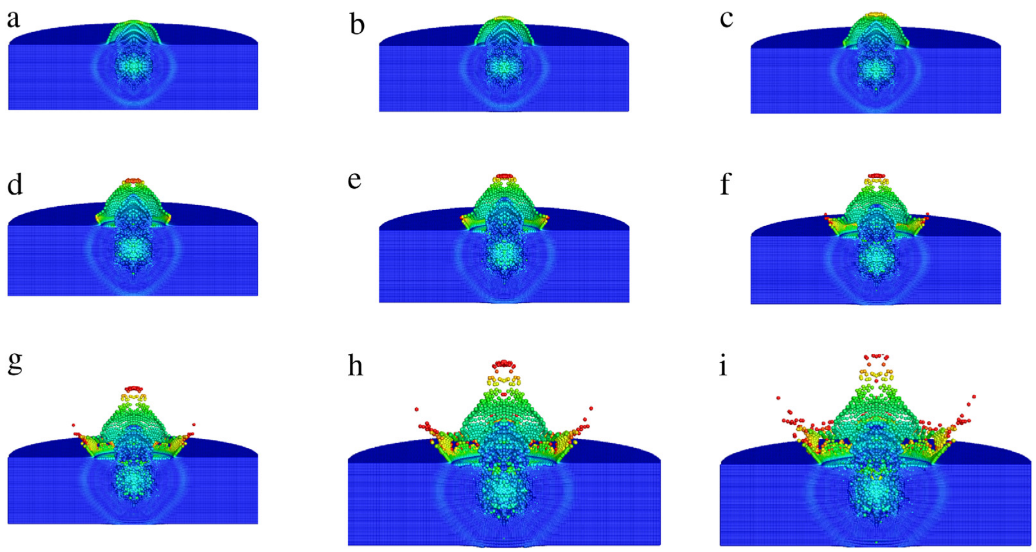

Fig. 20. Soil bubble evolution obtained from a two million particle simulation using the uncapped Drucker–Prager model. (The contour color represents the velocity magnitude.) (For interpretation of the references to color in this figure legend, the reader is referred to the web version of this article.)

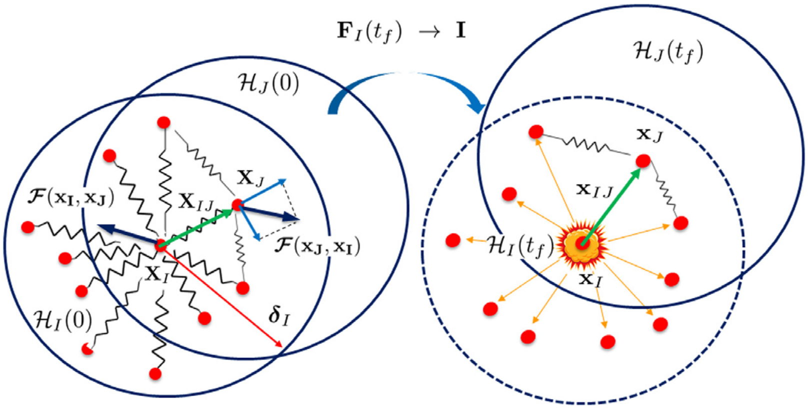

Fig. 21. Peridynamics soil particle cohesive and decohesion model: A nonlocal soft sphere becomes a local hard sphere during fragmentation.

say particle I, may sever all its bonds from the adjacent soil particles within its horizon (soft sphere), and the nonlocal soft sphere evolves to a rigid particle, or a local hard sphere with minuscule radius ($\delta_I = (3\Delta V_I/(4\pi))^{1/3}$) as shown in Fig. 21.[1] It is noted that by nonlocal soft sphere, we mean that there are neighboring particles inside the deformable sphere (horizon); by local hard sphere, we mean that there is no other particle inside or interact with the particle I, and the sphere cannot deform $\mathbf{F}_I = \mathbf{I}$.

The spring between two soil particles shown in Fig. 21 is in fact a cohesive-frictional spring, and its force–displacement relation may be derived from the Peridynamics force state by the following expression,

$$\mathcal{F}_{IJ}(\mathbf{F}_I) = \omega(X_{IJ})(\mathbf{P}_J - \mathbf{P}_I)(\mathbf{F}_I)\mathbf{K}_I^{-1} \cdot \mathbf{X}_{IJ}, \tag{99}$$

in which the first Piola–Kirchhoff stress may be derived from geomaterial constitutive model once the deformation gradient $\mathbf{F}_I$ is obtained. It may be noted that in the state-based Peridynamics, the bond force $\mathbf{f}_{IJ}$ in Eq. (99) looks like a pair force between the particles I and J, but it is in fact a nonlocal force representing the overall interaction

---

[1] This situation may change if we consider the recohesion.

surrounding the material bond $\mathbf{X}_{IJ}$. This is fundamentally different from the bond-based Peridynamics as well as DEM, in which the local pair force is used as the bond force.

During the soil fragmentation, if all the bonds of a particle, say particle I, are severed from its neighbors, we reset $\mathbf{K}_I = \mathbf{I}$ and $\mathbf{N}_I = \mathbf{I}$, and subsequently,

$$\mathbf{F}_I = \mathbf{I} \quad \rightarrow \quad \mathbf{P}_I = 0.$$

Moreover, if the bond between the particle pair IJ is severed, their interaction force state is set to zero as well, i.e. $\mathbf{f}_{IJ} = 0$, even though $\mathbf{P}_I$ and $\mathbf{P}_J$ may not be zero, because there may exist other soil particle bonds.

From Eq. (99), one may see that the role of the constitutive modeling is to provide the force–deformation relation for the Peridynamics nonlinear springs, which depends on soil constitutive models, no matter it is the Drucker–Prager model, or the Arenisca model. Moreover, the nonlinear spring force defined in Eq. (99) is not necessarily along the direction of $\mathbf{X}_{IJ}$ nor is it perpendicular to $\mathbf{X}_{IJ}$. One can see from Fig. 21 that this force has parallel component as well as perpendicular component to the direction $\mathbf{d}_{IJ} = \mathbf{X}_{IJ}/|\mathbf{X}_{IJ}|$, which may be interpreted as normal cohesive component as well as tangential cohesive and frictional component. In fact, for the state-based Peridynamics, one can show that if we sum all the bond force contributions from all the particles inside the horizon, the net force of tangential component will disappear [21]. There are two caveats of the present method: (1) The Peridynamics decohesion criterion only considers the normal bond breaking not the tangential bond breaking, and (2) The present method does not consider the re-cohesion, i.e. once a soil particle becomes a rigid body particle, it does not return to its "soft sphere" particle state. This treatment is sufficient for the simulation of soil fragmentation in the early and middle stage, but it is not capable of simulating dust particle falling off and settling after the explosion. Perhaps, a more advanced Peridynamics soil constitutive model is still needed in order to accurately predict the detailed decohesion/collision/re-cohesion process as well as the dynamic liquefaction process of soil media, e.g. [11,56].

The main part of this work is to use various geomaterial constitutive models to find the Peridynamics nonlinear spring force vector. As the numerical results indicate, however, if we use the same Peridynamics decohesion algorithm to break the bond, the general trends of soil fragmentation for different constitutive models are similar. Therefore, we think that it is the nonlocal state-based Peridynamics modeling and its corresponding decohesion bond breaking algorithm (criterion) that provide decisive advantages in both the modeling as well as the simulation of soil fragmentation. However, much work remains to be done to physically link the decohesion criterion or algorithm of the state-based Peridynamics with the geomaterial damage model.

Acknowledgments

This work was supported by an ONR MURI grant (No. N00014-11-1-0691). This support is gratefully appreciated. Moreover, we would like to thank: Richard Regueiro for providing us his Matlab subroutines of the Drucker–Prager models, Curt Hansen and Ronald Pak for the centrifuge testing data, and Eric Jensen and Rebecca Brannon for the discussions and information of the Arenisca soil model and the related geomaterial parameters.

Appendix A. Constitutive update for Drucker–Prager cap model

In this Appendix, we document the detailed computational algorithm in updating the stresses and other internal state variables (ISVs) when the yield function is tested to be greater than zero with the elastic trial stress. The stress and ISVs at time step n are provided, we need to obtain their corresponding values at time step $(n+1)$ by

$$\boldsymbol{\tau}_{n+1} = \boldsymbol{\tau}_n + \Delta t \mathbf{a} : (\mathbf{d} - \mathbf{d}^p) - \Delta\gamma \mathbf{a} : \frac{\partial g}{\partial \boldsymbol{\tau}} \tag{100}$$

$$\mathbf{q}^{\zeta}_{n+1} = \mathbf{q}^{\zeta}_n + \Delta\gamma \mathbf{h}^q, \tag{101}$$

subjected to the condition,

$$f_{n+1} = 0. \tag{102}$$

Eqs. (100)–(102) are a set of nonlinear equations, which can be solved by using the Newton–Raphson method. For the sake of clarity, in the following presentation, the subscript $(n+1)$ is left off.

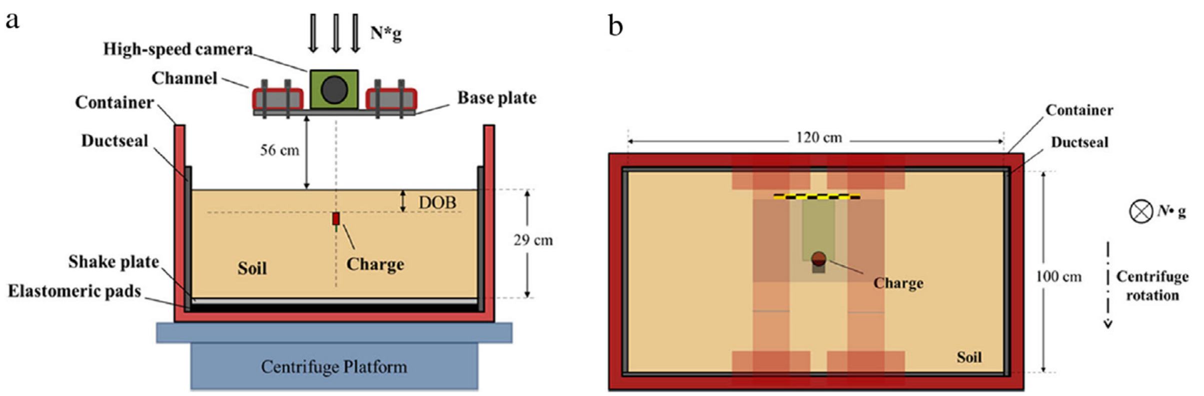

Fig. 22. Schematic illustration of the experimental layout for soil blasts experiments in the centrifuge: side (a) and top (b) view. *Source:* From Hansen and Pak [57].

Define a vector variable

$$\mathbf{X} = \begin{bmatrix} \boldsymbol{\tau} \\ \mathbf{q}^{\zeta} \\ \Delta\gamma \end{bmatrix}, \tag{103}$$

and a corresponding residual function of Eqs. (100)–(102)

$$\mathbf{R}(\mathbf{X}) = \begin{bmatrix} \mathbf{R}^{\tau} \\ \mathbf{R}^{q} \\ R^{\gamma} \end{bmatrix} = \begin{bmatrix} \boldsymbol{\tau} - \boldsymbol{\tau}_n - \Delta t\mathbf{a} : (\mathbf{d} - \mathbf{d}^p) + \Delta\gamma\mathbf{a} : \dfrac{\partial g}{\partial \boldsymbol{\tau}} \\ -\mathbf{q}^{\zeta} + \mathbf{q}^{\zeta}_n + \Delta\gamma\mathbf{h}^q \\ f \end{bmatrix} = \mathbf{0}. \tag{104}$$

One can linearize the residual **R** term for the unknown variable **X** as

$$\mathbf{R}^{k+1} = \mathbf{R}^{k} + \left.\frac{\partial \mathbf{R}}{\partial \mathbf{X}}\right|_k \cdot \delta\mathbf{X} \approx \mathbf{0}, \tag{105}$$

where

$$\frac{\partial \mathbf{R}}{\partial \mathbf{X}} = \begin{bmatrix} \dfrac{\partial \mathbf{R}^{\tau}}{\partial \boldsymbol{\tau}} & \dfrac{\partial \mathbf{R}^{\tau}}{\partial \mathbf{q}^{\zeta}} & \dfrac{\partial \mathbf{R}^{\tau}}{\partial \Delta\gamma} \\ \dfrac{\partial \mathbf{R}^{q}}{\partial \boldsymbol{\tau}} & \dfrac{\partial \mathbf{R}^{q}}{\partial \mathbf{q}^{\zeta}} & \dfrac{\partial \mathbf{R}^{q}}{\partial \Delta\gamma} \\ \dfrac{\partial R^{\gamma}}{\partial \boldsymbol{\tau}} & \dfrac{\partial R^{\gamma}}{\partial \mathbf{q}^{\zeta}} & \dfrac{\partial R^{\gamma}}{\partial \Delta\gamma} \end{bmatrix} = \begin{bmatrix} \mathbf{I} + \Delta\gamma\mathbf{a} : \dfrac{\partial^2 g}{\partial \boldsymbol{\tau}\partial \boldsymbol{\tau}} & \Delta\gamma\mathbf{a} : \dfrac{\partial^2 g}{\partial \boldsymbol{\tau}\partial \mathbf{q}^{\zeta}} & \mathbf{a} : \dfrac{\partial g}{\partial \boldsymbol{\tau}} \\ \Delta\gamma\dfrac{\partial \mathbf{h}^q}{\partial \boldsymbol{\tau}} & -\mathbf{1} + \Delta\gamma\dfrac{\partial \mathbf{h}^q}{\partial \mathbf{q}^{\zeta}} & \mathbf{h}^q\ . \\ \dfrac{\partial f}{\partial \boldsymbol{\tau}} & \dfrac{\partial f}{\partial \mathbf{q}^{\zeta}} & \mathbf{0} \end{bmatrix}. \tag{106}$$

For a given iteration k, we can first rewrite the first two equations as

$$\begin{bmatrix} \mathbf{R}^{\tau} \\ \mathbf{R}^{q} \end{bmatrix} + \mathbf{D} \cdot \begin{bmatrix} \delta\boldsymbol{\tau} \\ \delta\mathbf{q}^{\zeta} \end{bmatrix} + \delta(\Delta\gamma) \begin{bmatrix} \mathbf{a} : \dfrac{\partial g}{\partial \boldsymbol{\tau}} \\ \mathbf{h}^q \end{bmatrix} = \mathbf{0}, \tag{107}$$

where

$$\mathbf{D} = \begin{bmatrix} \mathbf{I} + \Delta\gamma\mathbf{a} : \dfrac{\partial^2 g}{\partial \boldsymbol{\tau}\partial \boldsymbol{\tau}} & \Delta\gamma\mathbf{a} : \dfrac{\partial^2 g}{\partial \boldsymbol{\tau}\partial \mathbf{q}^{\zeta}} \\ \Delta\gamma\dfrac{\partial \mathbf{h}^q}{\partial \boldsymbol{\tau}} & -\mathbf{1} + \Delta\gamma\dfrac{\partial \mathbf{h}^q}{\partial \mathbf{q}^{\zeta}} \end{bmatrix}. \tag{108}$$

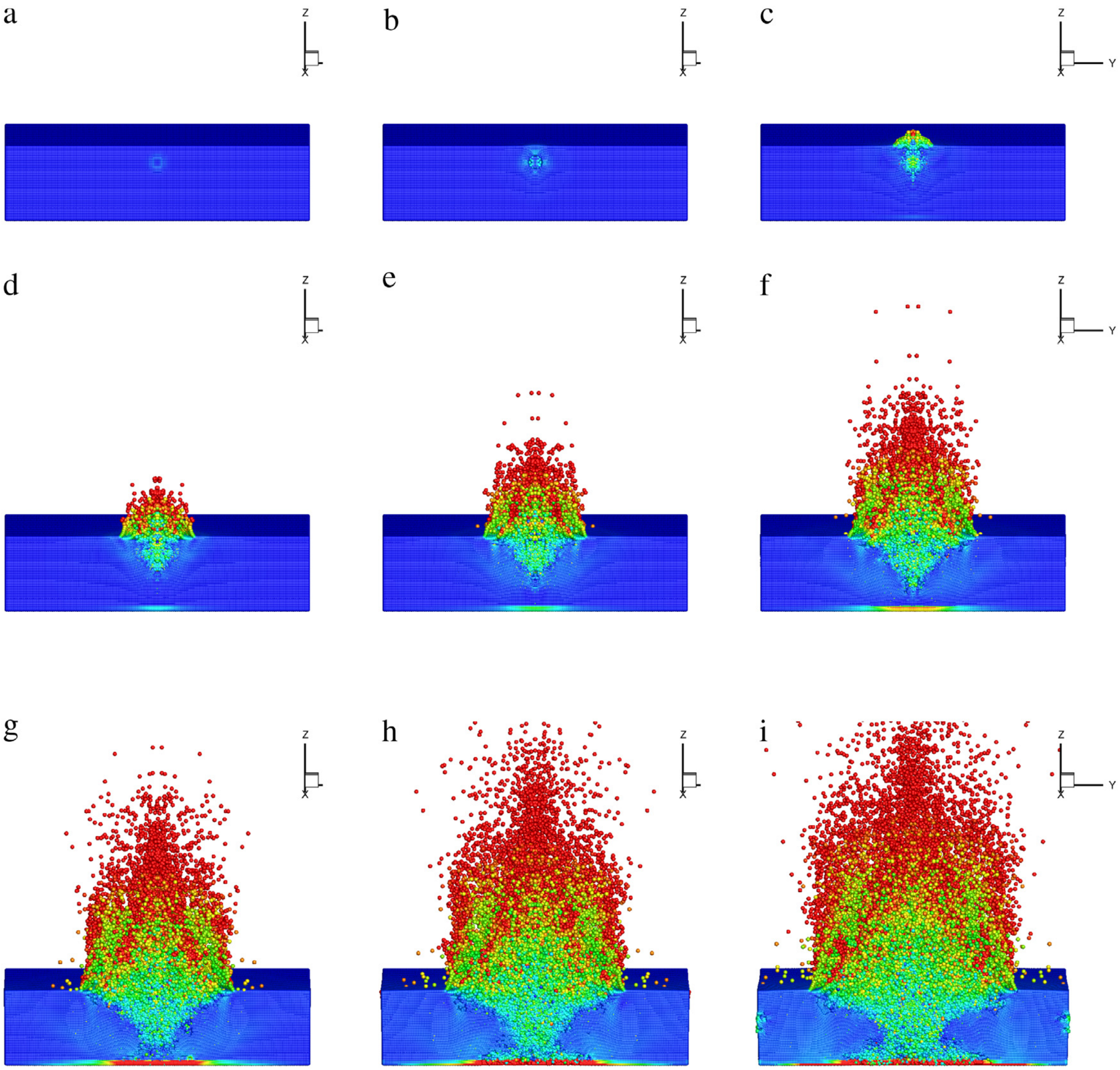

Fig. 23. Time sequence of the dynamic soil fragmentation in a Centrifuge simulated by using the Arenisca soil model. (The contour color represents the magnitude of velocity field.) (For interpretation of the references to color in this figure legend, the reader is referred to the web version of this article.)

Multiplying Eq. (107) by $\begin{bmatrix} \dfrac{\partial f}{\partial \boldsymbol{\tau}} & \dfrac{\partial f}{\partial \mathbf{q}^{\zeta}} \end{bmatrix} \cdot \mathbf{D}^{-1}$ from the left, and reorganizing the equation, one can obtain

$$\begin{aligned} &\delta(\Delta\gamma) \begin{bmatrix} \dfrac{\partial f}{\partial \boldsymbol{\tau}} & \dfrac{\partial f}{\partial \mathbf{q}^{\zeta}} \end{bmatrix} \cdot \mathbf{D}^{-1} \cdot \begin{bmatrix} \mathbf{a} : \dfrac{\partial g}{\partial \boldsymbol{\tau}} \\ \mathbf{h}^{q} \end{bmatrix} \\ &\quad = -\begin{bmatrix} \dfrac{\partial f}{\partial \boldsymbol{\tau}} & \dfrac{\partial f}{\partial \mathbf{q}^{\zeta}} \end{bmatrix} \cdot \mathbf{D}^{-1} \cdot \begin{bmatrix} \mathbf{R}^{\tau} \\ \mathbf{R}^{q} \end{bmatrix} - \begin{bmatrix} \dfrac{\partial f}{\partial \boldsymbol{\tau}} & \dfrac{\partial f}{\partial \mathbf{q}^{\zeta}} \end{bmatrix} \cdot \begin{bmatrix} \delta\boldsymbol{\tau} \\ \delta\mathbf{q}^{\zeta} \end{bmatrix}. \end{aligned} \tag{109}$$

Notice that

$$\begin{bmatrix} \dfrac{\partial f}{\partial \boldsymbol{\tau}} & \dfrac{\partial f}{\partial \mathbf{q}^{\zeta}} \end{bmatrix} \cdot \begin{bmatrix} \delta\boldsymbol{\tau} \\ \delta\mathbf{q}^{\zeta} \end{bmatrix} = -f. \tag{110}$$

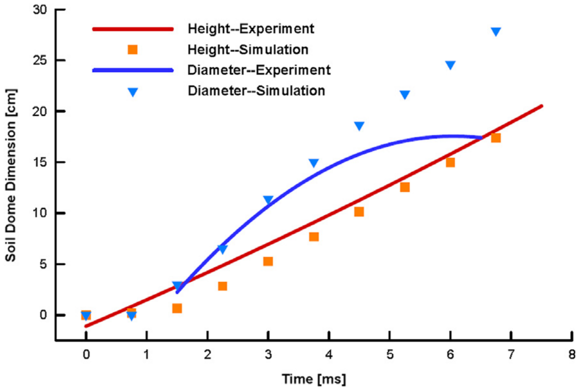

Fig. 24. Comparison of the soil bubble height and width between the results of numerical simulation and that of the Centrifuge test.

One can then solve the Newton–Raphson iteration increment for the time increment of the plastic multiplier as

$$\delta(\Delta\gamma) = \frac{f - \begin{bmatrix} \dfrac{\partial f}{\partial \boldsymbol{\tau}} & \dfrac{\partial f}{\partial \mathbf{q}^{\zeta}} \end{bmatrix} \cdot \mathbf{D}^{-1} \cdot \begin{bmatrix} \mathbf{R}^{\tau} \\ \mathbf{R}^{q} \end{bmatrix}}{\begin{bmatrix} \dfrac{\partial f}{\partial \boldsymbol{\tau}} & \dfrac{\partial f}{\partial \mathbf{q}^{\zeta}} \end{bmatrix} \cdot \mathbf{D}^{-1} \cdot \begin{bmatrix} \mathbf{a} : \dfrac{\partial g}{\partial \boldsymbol{\tau}} \\ \mathbf{h}^{q} \end{bmatrix}}. \tag{111}$$

By substituting Eq. (111) back into Eq. (107), one can obtain the update for the stress and ISVs as follows,

$$\begin{bmatrix} \delta\boldsymbol{\tau} \\ \delta\mathbf{q}^{\zeta} \end{bmatrix} = -\mathbf{D} \cdot \begin{bmatrix} \mathbf{R}^{\tau} + \delta(\Delta\gamma)\mathbf{a} : \dfrac{\partial g}{\partial \boldsymbol{\tau}} \\ \mathbf{R}^{q} + \delta(\Delta\gamma)\mathbf{h}^{q} \end{bmatrix}. \tag{112}$$

Appendix B. Experimental validation of the Arenisca model

The Arenisca soil model has been tested in various high strain rate shock wave loading conditions e.g. [24,44,46]. In this Appendix, we present the results of a Peridynamics numerical simulation of a centrifuge characterization of soil ejecta kinematics and crater morphology by using the state-based Peridynamics with the Arenisca model, hoping to validate the Peridynamics modeling by the centrifuge test results on dynamic soil responses under blast loading. A schematic illustration of the experiment setup layout for the soil blasts experiment is shown in Fig. 22, which is taken from [57], and a detailed description on the experiment setup can be also found in [57]. The dimension of the rectangular steel container is 1.2 m by 1.0 m by 0.61 m. The test makes use of a 1 g C4 charge, under a 5.1 cm DOB (Depth of Burial) overburden, and it is detonated at 1g level. The soil is modeled by using the Arenisca geomechanics model with all the material parameters listed in Table 2. The whole system is discretized into 2,954,902 particles. Time sequences of the explosion process is provided in Fig. 23. The evolution of the soil bubble shapes during the explosion process for both the numerical simulation and the corresponding experiments are shown in Fig. 24. One can see that the numerical and experiment curves have some margins within 30%–40% range, however they have shown similar trends. In Fig. 23(g) (h), and (i), one can clearly see the crater shape after the explosion, which is compared well with experiment results.

References

[1] J.L. Drake, C.D. Little Jr., Ground Shock from Penetrating Conventional Weapons, Technical Report, Army Engibeer Waterways Experiment Station, Vicksburg, MS, 1983.

[2] J. Wang, Simulation of a landmine explosion using LS-DYNA3D software, No. DSTO-TR116, Defence Science and Technology Organization Canberra (Australia), (2001).

[3] Z. Wang, Y. Lu, Numerical analysis on dynamic deformation mechanism of soils under blast loading, Soil Dyn. Earthq. Eng. 23 (2003) 705–714.

[4] Y. Lu. Z. Wang, K. Chong, A comparative study of buried structure in soil subjected to blast load using 2d and 3d numerical simulations, Soil Dyn. Earthq. Eng. 25 (2005) 275–288.

[5] X. Tong, C.Y. Tuan, Viscoplastic cap model for soils under high strain rate loading, J. Geotech. Geoenviron. Eng. 133 (2) (2007) 206–214.

[6] Z. Wang, Y. Lu. C. Bai, Numerical analysis of blast-induced liquefaction of soil, Comput. Geotech. 35 (2008) 196–209.

[7] M. Grujicic, B. Pandurangan, R. Qiao, B.A. Cheeseman, W.N. Roy, R.R. Skaggs, R. Gupta, Parameterization of the porous-material model for sand with different levels of water saturation, Soil Dyn. Earthq. Eng. 28 (2008) 20–35.

[8] Z.L. Wang, H. Konietzky, R.F. Shen, Coupled finite element and discrete element method for underground blast in faulted rock masses, Soil Dyn. Earthq. Eng. 29 (2009) 939–945.

[9] C.W. Watts, A.M. Tarquis, N.R.A. Bird, A.P. Whitmore, Modeling dynamic fragmentation of soil, Vadose Zone J. 8 (2009) 197–201.

[10] J. An, C.Y. Tuan, F. Asce, B.A. Cheeseman, G.A. Gazonas, Simulation of soil behavior under blast loading, Int. J. Geomech. 11 (2011) 323–334.

[11] Z. Wang, Y. Lu, C. Bai, Numerical simulation of explosion-induced soil liquefaction and its effect on surface structures, Finite Elem. Anal. Des. 47 (2011) 1079–1090.

[12] W.A. Charlie, T.E. Bretz, L.A. Schure (white), D.O. Doehring, Blast-induced pore pressure and liquefaction of saturated sand, ASCE J. Geotech. Geoenviron. Eng. 139 (8) (2013) 1308–1319.

[13] V.S. Deshpande, G.J. McShane, N.A. Fleck, A laboratory-scale buried charge simulator, Int. J. Impact Eng. 62 (2013) 210–218.

[14] M.G. Schumaker, J.P. Borg, G. Kennedy, N.N. Thadhani, Mesoscale simulations of dry sand, in: Dynamic Behavior of Materials, vol. 1, 2015, pp. 379–388.

[15] M.M. Crull, Buried Explosion Module(Bem): A Method for Determining the Fragment Hazards Due To Detonation of a Burid Munition, Technical Report, U.S. Army Engineering & Support Center, Huntsville, 1998.

[16] Z. Wang, Y. Lu, H. Hao, Numerical investigation of effects of water saturation on blast wave propagation in soil mass, J. Eng. Mech. 130 (2004) 551–561.

[17] B. Ren, H. Fan, G.L. Bergel, R.A. Regueiro, X. Lai, S. Li, A Peridynamics-SPH coupling approach to simulate soil fragmentation induced by shock waves, Comput. Mech. 55 (2015) 287–302.

[18] X. Lai, B. Ren, H. Fan, S. Li, C.T. Wu, A.R. Richard, L. Liu, Peridynamics simulations of geomaterial fragmentation by impulse loads, Int. J. Numer. Anal. Methods Geomech. 39 (2015) 189–213.

[19] H. Fan, G.L. Bergel, S. Li, A hybrid peridynamics-sph simulation of soil fragmentation by blast loads of buried explosive, Int. J. Impact Eng. 87 (2015) 14–27.

[20] S.A. Silling, Reformulation of elasticity theory for discontinuities and long-range forces, J. Mech. Phys. Solids 48 (2000) 175–209.

[21] S.A. Silling, M. Epton, O. Weckner, J. Xu, E. Askari, Peridynamic states and constitutive modeling, J. Elasticity 88 (2007) 151–184.

[22] D.C. Drucker, W. Prager, Soil mechanics and plastic analysis or limit design, Quart. Appl. Math. 10 (1952) 157–165.

[23] L. Resende, J.B. Martin, Formulation of Drucker–Prager cap model, J. Engrg. Mech. 111 (7) (1985) 855–881.

[24] B. Banerjee, R. Brannon, ONR-MURI Geomaterial Simulation Update Reports, (2015)–(2016).

[25] R.M. Brannon, A.F. Fossum, O.E. Strack, KAYENTA: Theory and User's Guide, Technical Report, Sandia National Laboratories at Albuquerque, NM and Livermore, CA, 2009.

[26] R.M. Brannon, M. Homel, E. Ghodrati, Arena: Theory and User's Guide, Technical Report, Department of Mechanical Engineering, University of Utah, Salt Lake City, UT, 2014.

[27] G.L. Bergel, S. Li, The total and updated Lagrangian formulation of state-based peridynamics, Comput. Mech. 58 (2016) 351–370.

[28] S. Li, W.K. Liu, Reproducing kernel hierarchical partition of unity Part I: Formulations, Internat. J. Numer. Methods Engrg. 45 (1999) 251–288.

[29] S. Li, W.K. Liu, Reproducing kernel hierarchical partition of unity Part II: Applications, Internat. J. Numer. Methods Engrg. 45 (1999) 289–300.

[30] W.-K. Liu, S. Li, T. Belytschko, Moving least square reproducing kernel method. (I) Methodology and convergence, Comput. Methods Appl. Mech. Engrg. 143 (1997) 113–154.

[31] F. Radjai, F. Dubois, Discrete-Element Modeling of Granular Materials, Wiley-Iste, 2011.

[32] S. Luding, Cohesive, frictional powders: Contact models for tension, Granular Matter 10 (4) (2008) 235–246.

[33] G.R. Liu, M.B. Liu, Smoothed Particle Hydrodynamics: A Meshfree Particle Method, World Scientific, 2003.

[34] D.A. Fulk, A Numerical Analysis of Smoothed Particle Hydrodynamics, (Ph.D. thesis), Air Force Institute of Technology, 1994.

[35] T. Rabczuk, T. Belytschko, S.P. Xiao, Stable particle methods based on Lagrangian kernels, Comput. Methods Appl. Mech. Engrg. 193 (12–14) (2004) 1035–1063.

[36] J.J. Monagphan, Simulating free surface flows with SPH, J. Comput. Phys. 110 (2) (1994) 339–406.

[37] M.B. Liu, G.R. Liu, K.Y. Lam, Z. Zong, Smoothed particle hydrodynamics for numerical simulation of underwater explosion, Comput. Mech. 30 (2) (2003) 106–118.

[38] D. Dooge, R. Dwarampudi, G. Schaffner, A. Miller, Evolution of occupant survivability simulation framwork using FEM-SPH coupling, in: 2011 NDIA Ground Vehicle Systems Engineering and Technology Symposium, Dearborn, Michigan, 2011.

[39] T.L. Warren, S.A. Silling, A. Askari, O. Weckner, M.A. Epton, J. Xu, A non-ordinary state-based peridynamic method to model solid material deformation and fracture, Int. J. Solids Struct. 46 (5) (2009) 1186–1195.

[40] J.T. Foster, S.A. Silling, W.W. Chen, Viscoplasticity using peridynamics, Internat. J. Numer. Methods Engrg. 81 (10) (2010) 1242–1258.

[41] M.R. Tupek, J.J. Rimoli, R. Radovitzky, An approach for incorporating classical continuum damage models in state-based peridynamics, Comput. Methods Appl. Mech. Engrg. 263 (2013) 20–26.

[42] L.H. Han, J.A. Elliott, A.C. Bentham, A. Mills, G.E. Amidon, B.C. Hancock, A modified Drucker–Prager Cap model for die compaction simulation of pharmaceutical powders, Int. J. Solids Struct. 45 (2008) 3088–3106.

[43] D. Bergeron, R. Walker, C. Coffey, Detonation of 100-Gram Anti-Personnel Mine Surrogate Charges in Sand-a Test Case for Computer Code Validation, Technical Report, Defence Research Establishment Suffield, Ralston ALTA (CAN), 1998.
[44] M.A. Homel, R.M. Brannon, J.E. Guilkey, Simulation of shaped-charge jet penetration into drained and undrained sandstone using the material point method with new approaches for constitutive modeling, in: International Center for Numerical Methods in Engineering, 2014.
[45] E. Jensen, Arenisca: Overview, ABAQUS Implementation and Parameter Calibration, Research Notes, 2014.
[46] M.A. Homel, J.E. Guilkey, R.M. Brannon, Continuum effective-stress approach for high-rate plastic deformation of fluid-saturated geomaterials with application to shaped-charge jet penetration, Acta Mech. 227 (2) (2016) 279–310.
[47] R.I. Borja, Cam-Clay Plasticity. Part V: A mathematical framework for three-phase deformation and strain localization analyses of partially saturated porous media, Comput. Methods Appl. Mech. Engrg. 193 (2004) 5301–5338.
[48] J.C. Simo, T.J.R. Hughes, Computational Inelasticity, Springer, 1997.
[49] T.J.R. Hughes, J. Winget, Finite rotation effects in numerical integration of rate constitutive equations arising in large-deformation analysis, Internat. J. Numer. Methods Engrg. 15 (1980) 1862–1867.
[50] B. Kilic, E. Madenci, An adaptive dynamic relaxation method for quasi-static simulations using the peridynamic theory, Theor. Appl. Fract. Mech. 53 (2010) 194–204.
[51] R. Regueiro, CVEN 6511 Lecture Notes: Nonlinear Finite Element Analysis of Solids and Porous Media, CU Boulder, University Lecture, 2007.
[52] G.A. Holzapfel, Nonlinear Solid Mechanics: A Continuum Approach for Engineering, Wiley, Chicjester, 2000.
[53] R. Courant, K. Friedrichs, H. Lewy, On the partial difference equations of mathematical physics, IBM J. 11 (1967) 215–234.
[54] R. Chandra, Parallel Programming in OpenMp, Morgan Kaufmann, 2001.
[55] H. Fan, S. Li., Parallel Peridynamics-SPH simulation of soil fragmentation by using OpenMP, Comput. Part. Mech. (2016). http://dx.doi.org/10.1007/s40571-016-0116-5. online.
[56] K. Sternik, F. Darve, Constitutive models for predicting liquefaction of soils, 18me Congrs Franais de Mcanique, Grenoble, 2007.
[57] C. Hansen, R.Y. Pak, Centrifuge characterization of buried, explosive-induced soil ejecta kinematics and crater morphology, J. Dyn. Behav. Mater. (2016) 1–20. Online.